Materials & Design 223 (2022) 110991

Contents lists available at ScienceDirect

Materials & Design

journal homepage: www.elsevier.com/locate/matdes

Technological implications of the Rosenthal solution for a moving point heat source in steady state on a semi-infinite solid

Mattia Moda *, Andrea Chiocca, Giuseppe Macoretta, Bernardo Disma Monelli, Leonardo Bertini

Department of Civil and Industrial Engineering, University of Pisa, Largo Lucio Lazzarino 2, 56122 Pisa, Italy

HIGHLIGHTS

- The feasibility of melting processes modeled by the Rosenthal solution is assessed.
- Closed-form expressions for the maximum velocity and optimal power are determined.
- Lack of fusion porosity of selective laser melted Inconel 718 is predicted.
- A basic procedure for narrowing the design space of powder bed fusion is proposed.

GRAPHICAL ABSTRACT

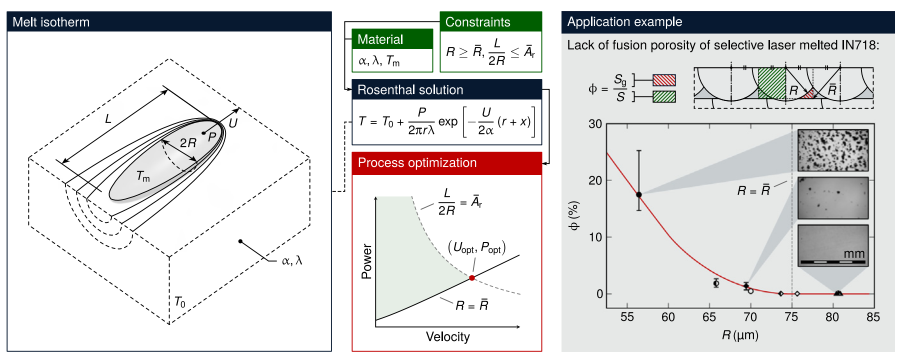

ARTICLE INFO

Article history:
Received 23 January 2022
Revised 20 July 2022
Accepted 24 July 2022
Available online 28 July 2022

Keywords:
Rosenthal solution
Welding
Additive manufacturing
Process optimization
Porosity

ABSTRACT

This paper introduces a theoretical framework for the analysis and optimization of melting processes that use focused moving heat sources. Specifically, we consider the Rosenthal solution for a moving point heat source in steady state on a semi-infinite solid. Firstly, we analyze the feasibility of the thermal problem while constraining the melt pool size and aspect ratio. We then express the maximum allowable velocity and the corresponding power as explicit functions of the constraints and material properties. Finally, we examine a wide range of melting processes within a dimensionless framework derived from the above solution. The paper concludes with an application example concerning lack of fusion porosity in powder bed fusion additive manufacturing, which shows the reliability of analytical estimates despite the complexity of the underlying physics. This makes it possible to outline a direct procedure for optimizing the main process parameters given a few basic requirements. Ultimately, the proposed methods are not intended to replace other modeling and experimental approaches, but rather to complement their capabilities and encourage more efficient use of available resources. In addition, reframing seemingly different problems within a common perspective can improve understanding, reveal new levels of similarity, and sometimes even allow for global solutions.

1. Introduction

Given their industrial relevance, welding and Additive Manufacturing (AM) have been the subject of extensive research. However, the question arises as to whether the overwhelming

* Corresponding author.
E-mail addresses: mattia.moda@ing.unipi.it (M. Moda), andrea.chiocca@phd.unipi.it (A. Chiocca), giuseppe.macoretta@phd.unipi.it (G. Macoretta), bernardo.monelli@ing.unipi.it (B.D. Monelli), leonardo.bertini@ing.unipi.it (L. Bertini).

https://doi.org/10.1016/j.matdes.2022.110991
0264-1275/

Nomenclature

$\bar{}$	Constrained quantity	T_0	Initial or preheating temperature
$\tilde{}$	Dimensionless quantity	T_m	Melting point
$\approx$	Approximate equality	U	Velocity magnitude
∇	Vector differential operator	U_opt	Optimal velocity magnitude
$\|\| \cdot \|\|$	Euclidean norm	$W_0(\cdot)$	Principal branch of the Lambert W function
A_r	Melt pool aspect ratio	X	x-coordinate of melt pool half-width R
d	Distance between adjacent scan lines	X^+	Maximum x-coordinate of the melt pool
L	Melt pool length	X^-	Minimum x-coordinate of the melt pool
ℓ	Characteristic length	x, y, z	Cartesian coordinates along $\hat{\boldsymbol{x}}, \hat{\boldsymbol{y}}, \hat{\boldsymbol{z}}$
P	Power	α	Thermal diffusivity
P_opt	Optimal power	β	Blending coefficient for R
R	Melt pool half-width	δR_e	Necking of the melt isotherm
r	Distance from the heat source	δT_e	End temperature perturbation
R_e	End curvature radius of the melt isotherm	ΔT_m	Temperature difference $T_\mathrm{m} - T_0$
Ry	Rykalin number	η	Blending coefficient for A_r
s	Nominal layer thickness	θ	Scanning direction angle
S_g	Tile gap cross-sectional area	λ	Thermal conductivity
T	Temperature	ϕ	Surface fraction of inter-bead gaps

amount of publications on the topic reflects its actual complexity or rather the lack of an overall perspective. After all, each material and technology has indeed its own peculiarities not to be overlooked, but assessing every case on an individual basis in a frantic search for novelty and specific solutions can be highly inefficient.

In response, analytical models are expressions of the will to understand, predict, and generalize experimental evidence within the limits of reason. This implies a propensity to simplification in apparent contrast to the continued development towards greater accuracy driven by the increase in data volume and computational resources. Nonetheless, the two approaches are not mutually exclusive. Closed-form solutions provide a clear overview of the main process parameters and outline their correlation with quality attributes. All this helps practitioners to narrow the design space while making it possible for researchers to minimize development efforts by generalizing the outcome of experimental and more elaborate modeling approaches.

The Rosenthal solution (Section 2) defines the thermal field produced by a moving point heat source in steady state on a semi-infinite solid. Despite its singularity, constant thermophysical properties, infinite substrate, and adiabatic boundary, it has repeatedly proven effective in modeling numerous melting processes [1–4]. Significant efforts have been made to improve the solution accuracy by introducing higher-order effects without sacrificing computational efficiency. In particular, the infinite substrate, adiabatic boundary, and axisymmetry assumptions can be worked around by combining heat sinks and multiple heat sources devised to model finite domains, surface heat loss, and keyhole mode melting [5–9]. Thermal transients and material nonlinearities are typically addressed via numerical integration or transform functions, while nonsingular solutions require distributed heat sources with finite heat flux densities [5,10,11]. In this case, however, we chose to prioritize simplicity over accuracy and analyzed the technological implications of the Rosenthal core solution with the aim of providing a basic theoretical framework for process engineering. It follows that our findings are instrumental for quantitative understanding and first-order assessments but should be subject to critical interpretation in view of the general research scope.

In summary, Section 3 describes a closed-form procedure to determine the optimal operating condition given two geometric constraints on the melt isotherm. Section 4 examines a broad range of welding and AM processes from a dimensionless perspective by factoring out scale and material dependencies. Lastly, Section 5 presents a practical application of the above solution for estimating lack of fusion porosity in powder bed fusion additive manufacturing.

2. Rosenthal solution

In the Eulerian reference frame of Fig. 1, the steady state thermal field produced by a point heat source moving on the surface of a semi-infinite solid has the following expression:

$$T = T_0 + \frac{P}{2\pi r \lambda} \exp\left[-\frac{U}{2\alpha}(r + x)\right] \tag{1}$$

where:

- T_0 is the initial temperature, which remains unchanged at an infinite distance from the heat source
- P is the thermal power transferred to the solid
- U is the velocity magnitude of the heat source relative to the solid

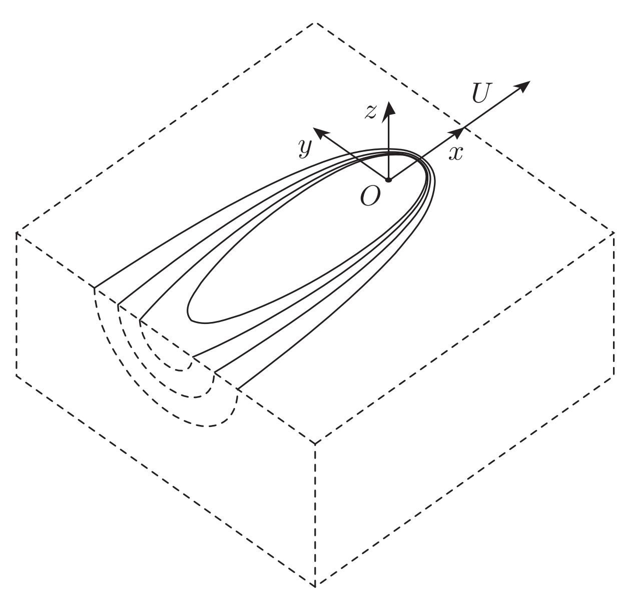

Fig. 1. Eulerian reference frame used to express the thermal field produced by a point heat source located at its origin O and moving along its x-axis with constant velocity of magnitude U relative to the semi-infinite solid $z \leqslant 0$.

- $r = \sqrt{x^2 + y^2 + z^2}$ is the distance from the heat source
- λ is the thermal conductivity
- α is the thermal diffusivity.

It should be noted that, given its axisymmetry about the axis of motion, Eq. (1) can represent the steady state thermal field produced by a point heat source moving on the apex of an infinite wedge of angle $\varphi \in (0, 2\pi]$, provided that P is multiplied by $\frac{\pi}{\varphi}$ [2]. Thus, the analysis and results presented in this section are applicable with minor adjustments to any thermal problem derived from or related to the above scenario.

The melt isotherm (Fig. 2), i.e., the isotherm of temperature $T = T_\mathrm{m} > T_0$, can be expressed as follows:

$$\frac{\ell}{r} \exp\left(-\frac{r+x}{\ell}\right) = \frac{1}{Ry} \tag{2}$$

where ℓ is the characteristic length:

$$\ell = \frac{2\alpha}{U} \tag{3}$$

and Ry is the Rykalin number [1,2]:

$$Ry = \frac{PU}{4\pi\lambda\alpha(T_\mathrm{m} - T_0)} \tag{4}$$

Of the two independent degrees of freedom, ℓ scales the melt isotherm, whereas Ry also affects its shape. However, neither is typically of practical use since the requirements and specifications for manufacturing processes involving localized melting are often expressed in terms of the size (e.g., width and penetration) and quality (e.g., limited distortions, inclusions, and porosity) of the melted zone. Conversely, the maximum half-width of the melt isotherm R and its aspect ratio A_r are two geometric quantities that are more meaningful in practice, as the former defines the transverse size of the melted zone, while the latter is inversely correlated with the weld quality (Section 3).

The thermal field defined by Eq. (1) is axisymmetric about the x-axis; hence, R represents both the half-width and penetration of the melted zone. It solves simultaneously Eq. (2) with $r = \sqrt{X^2 + R^2}$, where X is the x-coordinate of maximum width for the melt isotherm, and the derived constraint:

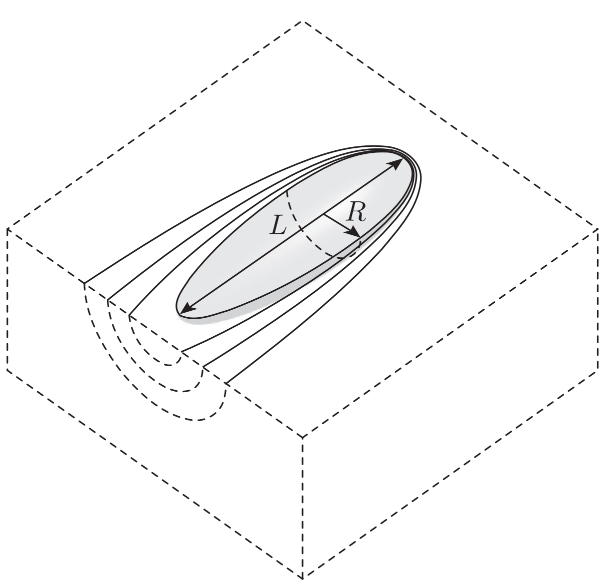

Fig. 2. Schematic representation of the melt isotherm $T = T_\mathrm{m}$ produced by a moving point heat source in steady state on a semi-infinite solid, where L and R are its maximum length and half-width, respectively.

$$\frac{\partial}{\partial x}\left[\frac{\ell}{\sqrt{x^2 + R^2}} \exp\left(-\frac{\sqrt{x^2 + R^2} + x}{\ell}\right)\right]\Bigg|_{x=X} = 0 \tag{5}$$

Although the system is not explicitly solvable for R and X, Wang et al. [1,2] retrieved the following approximated expressions:

$$R \approx \ell\, Ry \left[1 + \left(\frac{2}{\mathrm{e}\, Ry}\right)^{\beta/2}\right]^{1/\beta} \quad \text{with } \beta = -1.7312 \tag{6}$$

$$X \approx -\ell\, Ry^2 \left[1 + (\mathrm{e}\, Ry)^{0.999}\right]^{-1/0.999} \tag{7}$$

whose relative errors compared to the exact solutions are less than 0.7236% and 1.9051% for any value of Ry and tend to zero for either $Ry \to 0$ or $Ry \to \infty$.

The aspect ratio A_r is defined as the maximum length of the melt isotherm L divided by its maximum width $2R$. In particular, L is the difference between the two roots of Eq. (2) with $r = |x|$:

$$L = X^+ - X^- \tag{8}$$

where X^+ is related to Ry through the principal branch W_0 of the Lambert W function:

$$X^+ = \frac{\ell}{2} W_0(2\, Ry) \tag{9}$$

while:

$$X^- = -\ell\, Ry \tag{10}$$

It follows that:

$$A_\mathrm{r} = \frac{L}{2R} = \frac{\ell}{2R}\left[\frac{1}{2} W_0(2\, Ry) + Ry\right] \tag{11}$$

but given that R cannot be formulated explicitly, Wang et al. [2] retrieved an approximated expression also for A_r:

$$A_\mathrm{r} \approx \left[1 + \left(\frac{\mathrm{e}\, Ry}{8}\right)^{\eta/2}\right]^{1/\eta} \quad \text{with } \eta = 1.904 \tag{12}$$

whose relative deviation from the exact solution is less than 1.994% for any value of Ry and again tends to zero for either $Ry \to 0$ or $Ry \to \infty$.

3. Power-velocity optimization

We can now consider the problem of identifying the optimal operating condition for a generic melting process compliant with the Rosenthal solution. Our goal is to maximize the heat source velocity (and thus productivity) while satisfying the following constraints:

- the half-width or penetration of the melted zone must be greater than or equal to $\overline{R}$:

$$\ell\, Ry \left[1 + \left(\frac{2}{\mathrm{e}\, Ry}\right)^{\beta/2}\right]^{1/\beta} \geqslant \overline{R} \tag{13}$$

- the melt pool aspect ratio must be lower than or equal to $\overline{A}_\mathrm{r}$:

$$\left[1 + \left(\frac{\mathrm{e}\, Ry}{8}\right)^{\eta/2}\right]^{1/\eta} \leqslant \overline{A}_\mathrm{r} \tag{14}$$

While $\overline{R}$ is generally known a priori as a direct or indirect process requirement, identifying $\overline{A}_\mathrm{r}$ is often nontrivial and requires a trade-off between quality and productivity. After all, A_r is a property of the thermal field closely related to the melt pool and solidification dynamics, which in turn affect the resulting microstructure, porosity, and residual stresses. In the absence of stricter case-specific constraints, the Rayleigh-Plateau instability [12] limits A_r whenever bead uniformity is required. In fact, surface perturbations grow as the melt pool aspect ratio increases, eventually causing periodic beadlike protuberances known as BCM[1] humps [13]. This limits the productivity of highly automated manufacturing processes involving material melting via focused moving heat sources (including low-current GMAW[2], energy beam welding, and several AM technologies). Furthermore, surface perturbations negatively affect the bead quality, thus remaining a serious concern in semi-automatic and manual processes as well.

Another issue indirectly related to the aspect ratio is hot cracking, i.e., the genesis of shrinkage defects during the solidification of the weld bead. This can happen when local temperature variations cause the necking of the melt pool in its trailing portion. If such necking fragments the melt pool, the material solidifies in isolated hot spots with no liquid available to compensate for its shrinkage. This phenomenon is known to cause local concentrations of low-melting-point compounds (often containing impurities), which reduce the intergranular cohesion and may initiate cracking. The ensuing hot cracks are mostly longitudinal and grow under the tensile stresses arising throughout the cooling phase.

We can model the above phenomenon at the first order by considering a positive temperature drop δT_e occurring near the end of the melt pool. Such perturbation would cause a local necking δR_e of approximately:

$$\delta R_e \approx \frac{\delta T_e}{\|\nabla T|_{T=T_m}\|} \tag{15}$$

where $\|\nabla T|_{T=T_m}\|$ is the norm of the thermal gradient at solidification. As easily verifiable by deriving Eq. (1), the gradient norm at the end of the melt pool has the following expression:

$$\|\nabla T(-\ell\, Ry, 0, 0)\| = \frac{\Delta T_m}{\ell\, Ry} \tag{16}$$

where $\Delta T_m = T_m - T_0$ will be used hereinafter to improve readability. If we approximate by default the tail gradient norm with its end value, Eq. (15) becomes:

$$\delta R_e \approx \frac{\ell\, Ry\, \delta T_e}{\Delta T_m} \tag{17}$$

In addition, the trailing portion of the melt isotherm is locally approximated by a hemispherical surface of radius equal to the end curvature radius R_e:

$$R_e = \frac{\ell\, Ry}{1 + Ry} \tag{18}$$

obtainable from two derivations of Eq. (2). To prevent the local fragmentation of the melt pool, we must then simply impose $\delta R_e < R_e$, which by combining Eqs. (17,18) results in the following condition:

$$Ry < \frac{\Delta T_m}{\delta T_e} - 1 \tag{19}$$

Knowing the expected (process- and material-dependent) temperature drop δT_e, Eq. (12) allows to transfer the above constraint from Ry to A_r and thus identify the corresponding $\overline{A}_r$. Condition (19) suggests that, given a fixed T_0, the higher the melting point and process stability, the lower the susceptibility to hot cracking. Preheating (i.e., increasing T_0) reduces ΔT_m along with the thermal gradients and residual stresses [14], but it has an opposite effect on the risk of hot cracking.

[1] Beaded Cylinder Morphology.

[2] Gas Metal Arc Welding.

Additional technological constraints may introduce lower and upper bounds on the control variables [15], and either direct or indirect requirements on the transverse aspect ratio[3] of the melt pool may limit the energy density. Although these constraints were either not deemed applicable under the assumptions made or considered too case-specific to be generalized in accordance with the scope of our research, we provide some indications on how to include them later in this section.

Before solving the optimization problem, we define the dimensionless velocity:

$$\widetilde{U} = \frac{\overline{R}}{\ell} = \frac{U\overline{R}}{2\alpha} \tag{20}$$

and the dimensionless power:

$$\widetilde{P} = \frac{Ry}{\widetilde{U}} = \frac{P}{2\pi\lambda\overline{R}\Delta T_m} \tag{21}$$

to remove the problem's dependence on the selected $\overline{R}$. We then reformulate the inequality constraints (13,14) by replacing the control variables with their dimensionless counterparts:

$$\widetilde{P}\left[1 + \left(\frac{2}{e\widetilde{P}\widetilde{U}}\right)^{\beta/2}\right]^{1/\beta} \geqslant 1 \tag{22}$$

$$\left[1 + \left(\frac{e\widetilde{P}\widetilde{U}}{8}\right)^{\eta/2}\right]^{1/\eta} \leqslant \overline{A}_r \tag{23}$$

and combine them by making $\widetilde{U}$ explicit:

$$\widetilde{U} \leqslant \frac{2}{e\widetilde{P}} \min\left[\left(\widetilde{P}^{-\beta} - 1\right)^{-2/\beta}, 4\left(\overline{A}_r^{\eta} - 1\right)^{2/\eta}\right] \tag{24}$$

The resulting inequality defines the unbounded and non-convex feasible region exemplified in Fig. 3.

Considering the first quadrant of the $\widetilde{U}\widetilde{P}$-plane, which is the only physically meaningful region, the monotonically increasing bound (22) intersects the monotonically decreasing hyperbolic bound (23) at a single point of coordinates:

$$\widetilde{U}_{opt} \approx \frac{8}{e}\left(\overline{A}_r^{\eta} - 1\right)^{2/\eta}\left[1 + 2^{-\beta}\left(\overline{A}_r^{\eta} - 1\right)^{-\beta/\eta}\right]^{1/\beta} \tag{25}$$

$$\widetilde{P}_{opt} \approx \left[1 + 2^{-\beta}\left(\overline{A}_r^{\eta} - 1\right)^{-\beta/\eta}\right]^{-1/\beta} \tag{26}$$

where $\widetilde{U}_{opt}$ is the maximum dimensionless velocity achievable for the given $\overline{A}_r$. This implies that the above intersection point, whose dimensional coordinates are obtainable by inverting Eqs. (20,21):

$$U_{opt} \approx \frac{2\alpha}{\overline{R}}\widetilde{U}_{opt} \tag{27}$$

$$P_{opt} \approx 2\pi\lambda\overline{R}\Delta T_m\widetilde{P}_{opt} \tag{28}$$

constitutes the optimal operating condition for maximizing productivity while satisfying the specified constraints. As it is located at a vertex of the feasible region, the calculated condition is unreliable since even slight variations of power (or an increase in velocity) would produce a constraint violation. Thus, the selected velocity should be lower than U_{opt} by a factor of safety, which depends on the expected accuracy and a case-specific trade-off between quality and productivity.

As represented in Fig. 4, both $\widetilde{U}_{opt}$ and $\widetilde{P}_{opt}$ increase with $\overline{A}_r$, and the feasible region widens, thus allowing higher velocities provided that the heat source power is increased to prevent constraint (22) from being violated. At some point, however, additional issues

[3] I.e., the ratio between the depth and width of the melted zone.

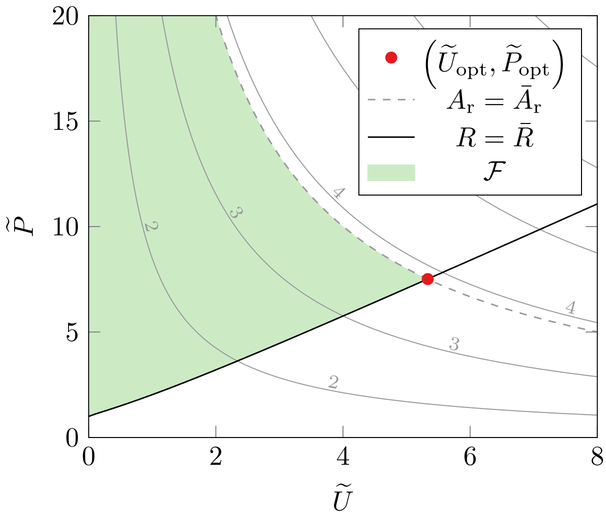

Fig. 3. Exemplified representation of the feasible region $\mathcal{F}$ and optimal operating condition. The contour map shows the hyperbolic isolines of aspect ratio.

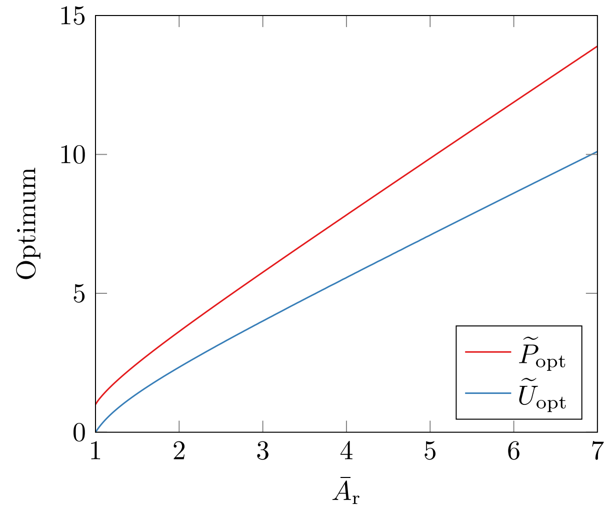

Fig. 4. Dimensionless power and velocity corresponding to the optimal operating condition varying the maximum allowable aspect ratio.

may render the optimal operating condition less cost-effective than other suboptimal solutions. For example, box-type, linear, and nonlinear technological constraints on U and P may restrict the feasible region making $(U_{\mathrm{opt}}, P_{\mathrm{opt}})$ infeasible in practice [16]. Another issue may arise at low $\bar{A}_{\mathrm{r}}$, as when the optimal operating condition gets closer to $(0, 1)$ on the $\widetilde{U}\widetilde{P}$-plane, the energy density increases, and the evaporation recoil pressure reshapes the melt pool into a keyhole. In fact, since the energy density is always directly proportional to P and inversely proportional to U regardless of the specific formulation, its value approaches infinity as the velocity gets arbitrarily close to zero with finite power. If (U, P) are the only variables, and the energy density is considered the discriminating factor between conduction and keyhole mode melting, the transition region between those regimes should be representable as an angle on the $\widetilde{U}\widetilde{P}$-plane (as the lines passing through the origin of that plane have constant energy densities proportional to their gradients). In that case, the lower side of such angle constitutes the theoretical limit of applicability of the Rosenthal solution (1), which is not suitable for modeling the keyhole formation without combining multiple heat sources[4]. It follows that the feasible region (24) is unbounded simply because the considered mathematical model is not affected by a generalized constraint on the transverse aspect ratio of the melt pool, which instead is always present in practice.

Ultimately, it is not completely fair to consider the thermal problem independent of the length scale, as many phenomena, including the melt pool stability, microstructure evolution, and surface heat transfer effectiveness relative to conduction, are notoriously scale-dependent. However, additional or scale-dependent inequality constraints may affect the shape and size of the feasible region (possibly precluding the use of dimensionless variables) but not the overall problem structure. Therefore, the optimization problem remains inherently two-dimensional (unless any inequality constraint is maintained active, making it an equality constraint), and any scalar reduction ends up providing only a section view of the whole picture, which instead can be fully examined using two independent variables.

4. Exploratory data analysis

We examined a broad spectrum of manufacturing processes under the unified theoretical framework defined in Section 3. Specifically, our exploratory data analysis covered Arc and Beam[5] Welding (AW and BW, respectively) on various materials, joint types, and bead sizes ranging from 0.5 to over 10 mm. As for AM technologies, we considered[6] Laser Metal Deposition (LMD) and Selective Laser Melting (SLM) but not Electron Beam Melting (EBM) due to the lack of information about the process parameters. Despite being limited by the assumptions of the Rosenthal solution, the proposed approach could still serve as a baseline for assessing several applications that would technically fall out of its scope without proper adjustments, including keyhole mode welds and additively manufactured parts of feature size comparable to the process resolution.

Fig. 5 shows the dimensionless operating conditions selected from reviewing the publications in Table 1. Each nominal operating condition is marked with a symbol and a color corresponding to the process type and processed material, respectively. The error bars represent the estimated power losses due to the process- and material-dependent energy absorptivity (or efficiency), which is rarely known in practice. In fact, P is defined as the thermal power transferred to the solid, and its difference compared to the nominal power constitutes the main uncertainty in locating each operating condition on the $\widetilde{U}\widetilde{P}$-plane. However, a simple yet effective way of reducing this uncertainty would be to measure R experimentally and then estimate P by inverting Eqs. (4,6).

The hyperbolic isolines of A_{r} (Fig. 3) become linear in logarithmic scale, and, apart from some outliers, the operating conditions appear evenly distributed above constraint (22) within the range $1.1 \leqslant A_{\mathrm{r}} \leqslant 7$. A closer look reveals that AW rarely exceeds $A_{\mathrm{r}} = 2$, whereas BW and LMD are generally limited to $A_{\mathrm{r}} \leqslant 3$ (with some rare exceptions still lower than $A_{\mathrm{r}} = 4$). On the other hand, the range above $A_{\mathrm{r}} = 3$ is dominated by the SLM process, whose operating conditions extend even beyond $A_{\mathrm{r}} = 7$. This is likely due to the higher priority given to productivity over quality in AM compared to welding. In fact, a typical SLM process can comprise millions of scan lines, and the quality of a single weld bead has little to

[4] To break the axisymmetry of the thermal field about the axis of motion [8,9].

[5] Including both Laser and Electron Beam Welding, commonly abbreviated as LBW and EBW, respectively.

[6] By limiting the research to the last five years of published literature in an attempt to provide an up-to-date overview of metal AM technologies.

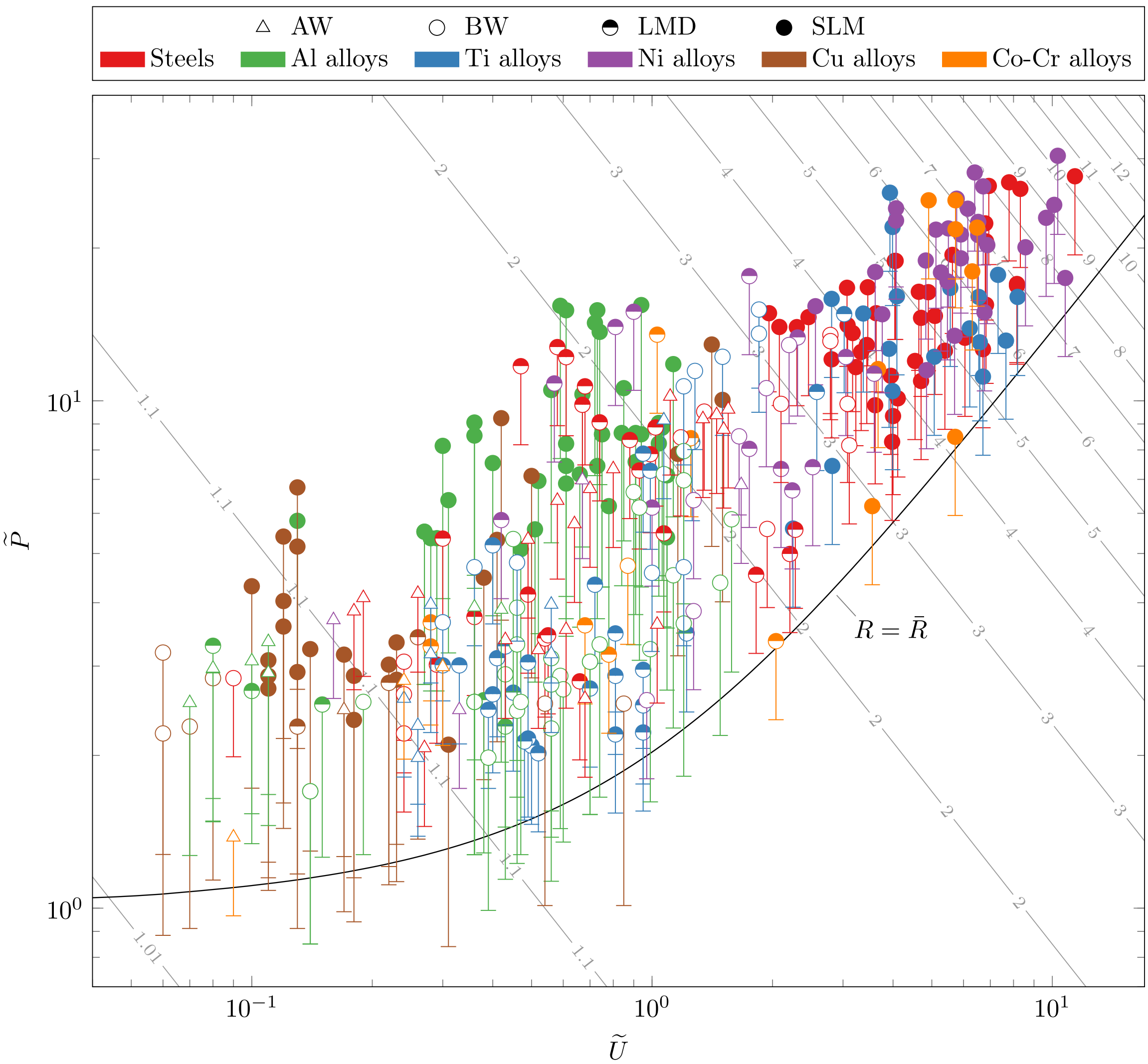

Fig. 5. Dimensionless nominal operating conditions retrieved from the reviewed literature (Table 1). The error bars represent the estimated power losses, i.e., the power fractions not contributing to the heating process. The solid line $R = \overline{R}$ is the feasibility boundary defined by the dimensionless constraint (22), while the contour map shows the isolines of aspect ratio.

Table 1
Summary of the reviewed literature. Manufacturing processes are classified into four categories: Arc Welding (AW), Beam Welding (BW), Laser Metal Deposition (LMD), and Selective Laser Melting (SLM); materials are classified based on the main alloy elements into six macro-categories and, where appropriate, additional sub-categories.

Material		Process			
Category	Properties	AW	BW	LMD	SLM
Structural steel	[17–24]	[17,18,20,23,25–32]	[32–36]		
Stainless steel	[28,37–42]	[18,43–45]	[41,46]	[47–57]	[58–75]
Tool steel	[76,77]			[78]	[61,79–86]
Maraging steel	[87]				[61,88–95]
Al2xxx	[96]		[96–102]	[103]	[104,105]
Al4xxx	[106]		[107,108]		[109–123]
Al5xxx	[124–126]	[125]	[127,128]	[129,130]	[131–137]
Al6xxx	[138]	[139,140]	[141–146]		[113]
Al7xxx	[147]	[148,149]		[150]	[151–153]
Ti alloys	[154,155]	[156,157]	[155,158–163]	[164–182]	[183–200]
Ni alloys	[201–204]	[205,206]	[207,208]	[209–216]	[172,217–241]
Cu alloys	[242–244]	[245]	[245–248]	[249–251]	[94,252–270]
Co-Cr alloys	[271,272]	[273–275]	[276]	[214,277–281]	[226,282–288]

Table 2
Thermophysical properties of Inconel 718 alloy [291].

Property	Value
Thermal conductivity	25 W m^{-1} K^{-1}
Thermal diffusivity	5 $\times$ 10^{-6} m^2 s^{-1}
Melting point	1538 K
Energy absorptivity[7]	0.7

[7] Estimated by measuring the bead size.

no effect on the quality of the entire manufactured part, provided that porosity is kept within the prescribed tolerance. Conversely, bead quality standards are generally higher in welding at the expense of productivity. Moreover, a higher degree of automation and control often corresponds to a higher allowable A_r, which in turn must be exploited to recover the additional costs associated with the potential increase in productivity.

The above considerations apply when comparing different process types for the same material. However, focusing on each type separately and comparing the operating conditions for different materials leads to further interesting observations. In particular, the behavior of Cu- and Al-based alloys can be clearly distinguished from that of other materials, which, despite their different thermophysical and mechanical properties, have similar distributions on the $\widetilde{U}\widetilde{P}$-plane.

Copper alloys typically have lower absorptivities and higher thermal conductivities than the other materials considered here. Therefore, as we can infer from Eqs. (26,28), they require significantly higher nominal powers for the same $\overline{R}$ and $\overline{A}_r$, which makes them more likely to saturate the available power sources. In addition, Cu alloys are less commonly used (and thus less developed) than most others, and together these factors lead to the lower aspect ratios currently achievable with the same process types.

On the other hand, aluminium alloys are among the most widely used, despite also having the absorptivity and thermal conductivity issues mentioned above. Nonetheless, even the most productivity-oriented SLM processes rarely exceed an aspect ratio of two with Al alloys, while they easily achieve values three times higher with other non-copper alloys. Our guess is that hot cracking

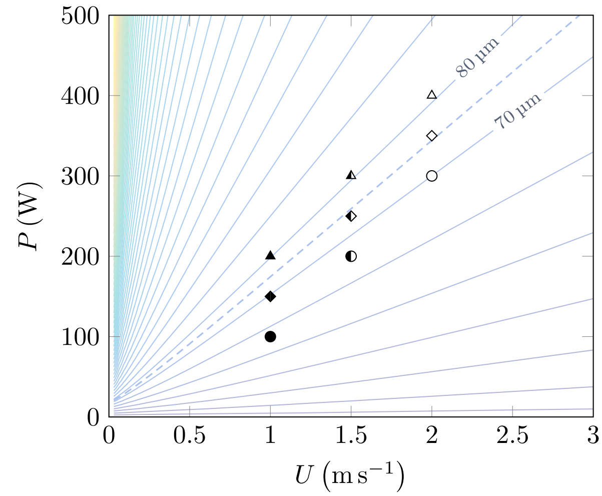

Fig. 7. Tested nominal operating conditions. The contour map shows the theoretical isolines of R (dashed for $R = \overline{R}$) based on Eq. (6) and the input data listed in Tables 2,3.

[105,152,289] may constitute the main hindrance due to the low melting point. In fact, BCM humping limits the processability of other materials at much higher aspect ratios, whereas the low ΔT_m (especially in case of significant preheating) combined with the large grain size of Al alloys [153] may anticipate the onset of hot cracking (19) at $Ry \approx 10$ (or equivalently, $A_r \approx 2$). Mitigating this issue [104] and compensating for the evaporation of highly volatile alloying elements (mainly Mg and Zn [122,131]) should thus be considered essential prerequisites for increasing the productivity and viability of AM technologies on aluminium alloys.

5. Application on lack of fusion porosity

To showcase the practical utility of the analytical approach presented in previous sections, we will now address the issue of pre-

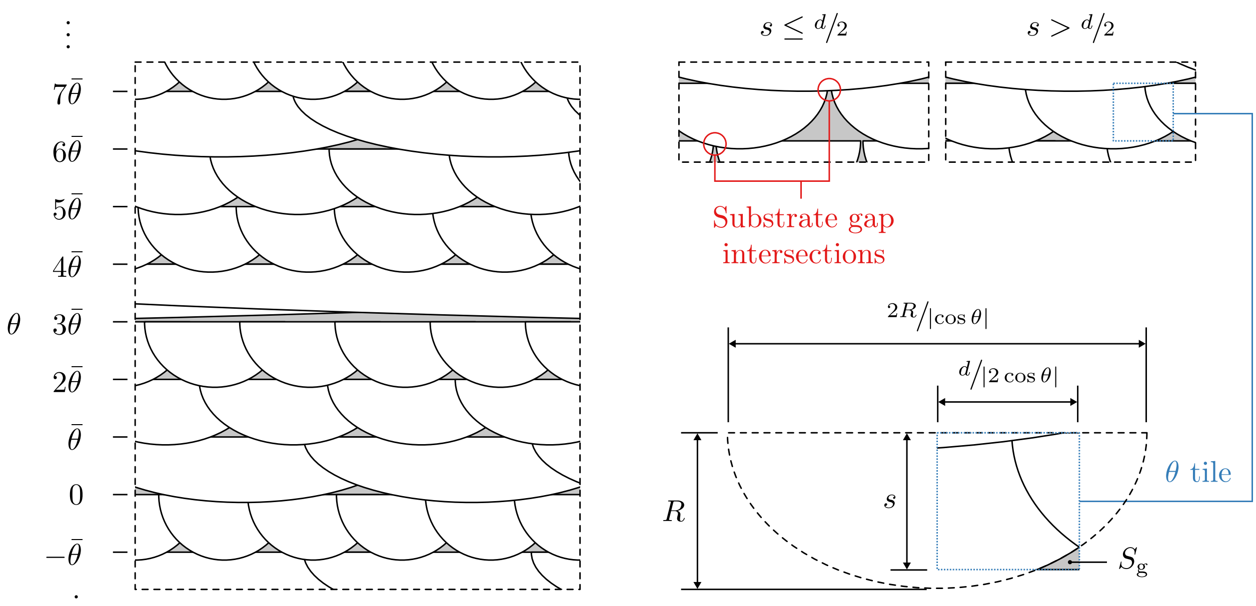

Fig. 6. Cut surface of a specimen printed with uniform hemicylindrical beads of radius R and a hatch angle $\bar{\theta}$ of 67°. Substrate gap intersections may occur if the nominal layer thickness s is less than half of the hatch distance d. Otherwise, the gap fraction of the entire cut surface is the same as that of any tile $\frac{d}{2|\cos\theta|} \times s$ with a top vertex on the respective scan line.

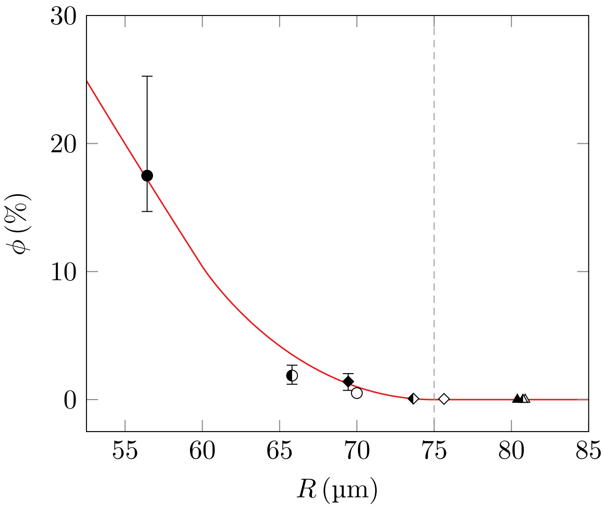

Fig. 8. Predicted and measured lack of fusion porosity for the nine operating conditions represented in Fig. 7 (error bars are omitted if smaller than the respective marker).

venting lack of fusion porosity in Powder Bed Fusion (PBF) additive manufacturing. Specifically, we consider the selective laser melting of Inconel 718 (thermophysical properties in Table 2) using a Renishaw RenAM 500E on a commercial powder compliant with the ASTM F3055 standard [290].

Table 3
Pre-set SLM process parameters for Inconel 718.

Parameter	Value
Nominal layer thickness	60 μm
Hatch distance	90 μm
Hatch angle[8]	67°
Preheating temperature	541 K

[8] Angle between the scanning directions of two consecutive layers.

Lack of fusion porosity can be estimated as the surface fraction of inter-bead gaps ϕ. As exemplified in Fig. 6, if R is constant, and the nominal layer thickness s (i.e., the distance increment between the recoater and the base plate) is greater than half of the hatch distance d (i.e., the distance between adjacent scan lines), hemicylindrical beads cannot intersect the inter-bead gaps of underlying layers. In this case, ϕ is the same for any cutting plane of normal unit vector $\hat{\boldsymbol{n}}$ perpendicular to the build direction, and the cut surface consists of layered tiles with horizontal stretch factor $\frac{1}{|\cos\theta|} = |\sec\theta|$, where θ is the scanning direction angle relative to $\hat{\boldsymbol{n}}$. It follows that, as the tile gap cross-sectional area $S_g(\theta) = |\sec\theta| S_g(0)$:

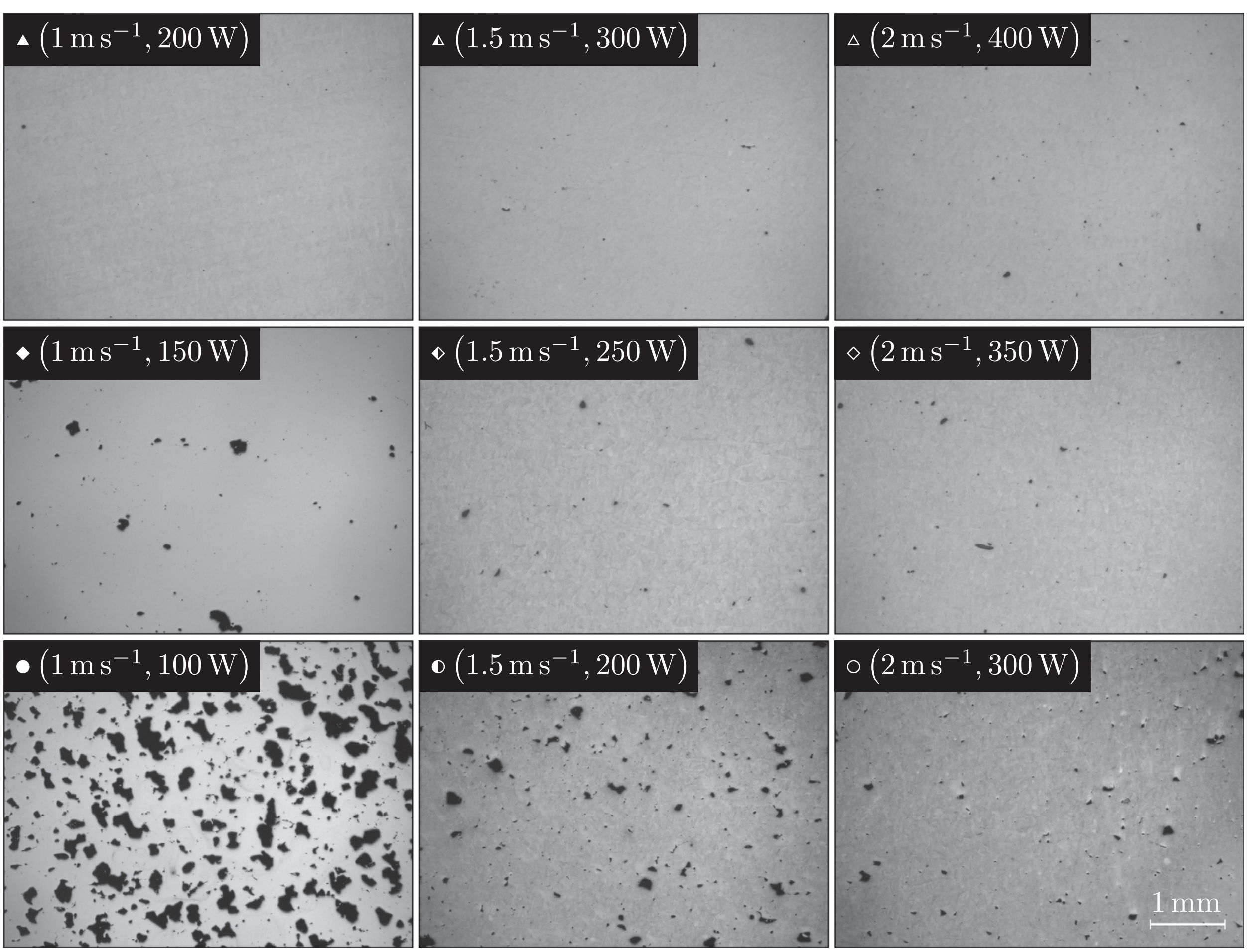

Fig. 9. Cross-section photomicrographs of selective laser melted Inconel 718 with vertical build direction. The nine specimens were printed using the nominal operating conditions (U, P) represented in Fig. 7 and the process parameters listed in Table 3. Kalling's reagent II was used to detect bead boundaries on less porous surfaces, which made it easier to distinguish lack of fusion from gas entrapment.

$$\phi = \frac{2S_g(\theta)}{|\sec\theta|ds} = \frac{2S_g(0)}{ds} \tag{29}$$

and the value of ϕ for the entire cut surface can be calculated considering a single tile with $\theta = 0$:

$$\phi = \begin{cases} 1 - \frac{\pi R^2}{2ds} & \text{if } R \leqslant \frac{d}{2} \\ 1 - \frac{R_1}{2s} - \frac{R^2}{ds}\arctan\left(\frac{d}{2R_1}\right) & \text{if } \frac{d}{2} < R \leqslant s \\ 1 - \frac{R_1}{2s} - \frac{R_2}{d} - \frac{R^2}{ds}\left[\arctan\left(\frac{d}{2R_1}\right) - \operatorname{arccot}\left(\frac{s}{R_2}\right)\right] & \text{if } s < R \leqslant \overline{R} \\ 0 & \text{otherwise} \end{cases} \tag{30}$$

where $R_1 = \sqrt{R^2 - \frac{d^2}{4}}$, $R_2 = \sqrt{R^2 - s^2}$, and $\overline{R} = \sqrt{s^2 + \frac{d^2}{4}}$.

Fig. 8 shows the comparison between the predicted and measured lack of fusion porosity for the nine operating conditions represented in Fig. 7. Each operating condition was used to print its corresponding specimen (Fig. 9) with the process parameters listed in Table 3, which made the above formulation applicable since $s = 60\,\mu\text{m}$ is greater than $\frac{d}{2} = 45\,\mu\text{m}$. Despite the simplicity of the model, its predictions were generally accurate with minor overestimations of ϕ in the range $65\,\mu\text{m} \leqslant R \leqslant 70\,\mu\text{m}$, which likely resulted from the actual bead shapes not being hemicylindrical as assumed. Most importantly, the theoretical full-density threshold $R \geqslant \overline{R} = 75\,\mu\text{m}$ delimited all operating conditions associated with negligible lack of fusion porosity.

The result quality should always be assessed in relation to the process variability. In this specific case, we limited the model uncertainty by estimating the energy absorptivity across a wide range of process parameters. In particular, we sampled multiple melted zones for each operating condition, computed their average radius via least-squares circle fitting, solved Eq. (6) for Ry, determined P from Eq. (4), and divided its value by the nominal power, which resulted in an average absorptivity of 0.7 consistent with the available data [292]. However, while computing the best-fit circle radii, we observed a 14% coefficient of variation that roughly represents the maximum accuracy achievable without taking into account the local differences between nominally identical scan lines. This intrinsic limitation of the model, combined with the practical inability to reproduce the actual bead shapes and powder distribution relative to the inter-bead gaps, make predicting incidental porosity features virtually impossible at present. Nevertheless, the agreement with experimental evidence suggests that, presumably owing to their non-systematic nature, most of the above errors (apart from assuming hemicylindrical bead shapes) are only marginally reflected in the estimated ϕ.

Based on these final considerations, we could outline the following procedure for setting up a generic PBF process:

1. Select s and $\overline{A}_r$ as a trade-off between resolution, quality, and productivity
2. Compute $\overline{R} = \sqrt{2}s$ considering $\frac{d}{2} = s$
3. Compute Ry by inverting Eq. (12) with $A_r = \overline{A}_r$
4. Select the maximum allowable preheating temperature to limit residual stresses without incurring the risk of hot cracking (19), i.e., $T_0 < T_m - \delta T_e(Ry + 1)$
5. Compute $\widetilde{U}_{opt}$ and $\widetilde{P}_{opt}$ from Eqs. (25,26)
6. Compute U_{opt} and P_{opt} from Eqs. (27,28)
7. Determine the nominal power by dividing P_{opt} by the expected energy absorptivity
8. Adjust s and d at constant $\overline{R}$ according to the actual bead shape (which is mainly dependent on the energy density), i.e., reduce d relative to s nearing the keyhole mode and vice versa.

Needless to say, the selected s, $\overline{A}_r$, and T_0, as well as the resulting operating condition, must comply with the case-specific technological constraints, and parameter fine-tuning may still require structured experimental approaches.

6. Conclusions

We presented a closed-form procedure to determine the optimal operating condition for melting processes compliant with the Rosenthal solution. The derived framework enabled us to compare welding and AM processes from a dimensionless perspective and appreciate the remarkable similarities between the reframed operating conditions for a wide range of materials. In addition, the literature data analysis combined with a few theoretical considerations led us to identify hot cracking as possibly the main hindrance to productivity for additive manufacturing of aluminium alloys. On a more practical level, we estimated the void surface fraction of selective laser melted Inconel 718 based solely on the Rosenthal solution and concluded by outlining a basic procedure for setting up PBF processes.

Our research shows that, despite being often overlooked in favor of experimental and more elaborate modeling approaches, analytical solutions provide a clear insight into the multidimensional design space underlying most welding and AM technologies. As such, the Rosenthal solution is inherently well suited for educational purposes, explanatory and exploratory data analyses, feasibility and sensitivity analyses, and all applications where usability and performance are to be prioritized over accuracy and flexibility. Most notably, if calibrated through a few simple measurements, it can provide guidance for experimental procedures in process optimization and serve as internal model for industrial control systems.

In the end, even with the limitations it entails, simplicity remains a decisive advantage in the vast majority of practical cases.

Data availability

The data that support the findings of this study are openly available in Mendeley Data at https://doi.org/10.17632/b2437352ky.2, reference number 10.17632/b2437352ky.2.

Declaration of Competing Interest

The authors declare that they have no known competing financial interests or personal relationships that could have appeared to influence the work reported in this paper.

Acknowledgements

The authors express their gratitude to Franco Bonollo and Paolo Ferro from the University of Padova, who provided insight and expertise in the interpretation of the reviewed literature on aluminium alloys.

References

[1] P.F. Mendez, Y. Lu, Y. Wang, Scaling analysis of a moving point heat source in steady-state on a semi-infinite solid, J. Heat Transf. 140 (8) (2018) 081301, https://doi.org/10.1115/1.4039353.
[2] Y. Wang, Y. Lu, P.F. Mendez, Scaling expressions of characteristic values for a moving point heat source in steady state on a semi-infinite solid, Int. J. Heat Mass Transf. 135 (2019) 1118–1129, https://doi.org/10.1016/j.ijheatmasstransfer.2019.02.042.
[3] D.C. Saha, D. Westerbaan, S.S. Nayak, E. Biro, A.P. Gerlich, Y. Zhou, Microstructure-properties correlation in fiber laser welding of dual-phase and HSLA steels, Mater. Sci. Eng. A 607 (2014) 445–453, https://doi.org/10.1016/j.msea.2014.04.034.

[4] J. Li, Q. Wang, P. Michaleris, E.W. Reutzel, Model prediction for deposition height during a direct metal deposition process, 2017 American Control Conference (ACC) (2017) 2188–2194, https://doi.org/10.23919/ACC.2017.7963277.

[5] H.S. Carslaw, J.C. Jaeger, Conduction of Heat in Solids, 2nd Edition, Oxford University Press (1959).

[6] J. Ning, W. Wang, B. Zamorano, S.Y. Liang, Analytical modeling of lack-of-fusion porosity in metal additive manufacturing, Appl. Phys. A 125 (11) (2019) 797, https://doi.org/10.1007/s00339-019-3092-9.

[7] J. Ning, D.E. Sievers, H. Garmestani, S.Y. Liang, Analytical modeling of part porosity in metal additive manufacturing, Int. J. Mech. Sci. 172 (2020) 105428, https://doi.org/10.1016/j.ijmecsci.2020.105428.

[8] L. Romoli, A. Musacchio, A. Franco, M.C. Fierro, G. Dini, A double-point moving source model for predicting seam geometry in laser welding, CIRP Ann. 62 (1) (2013) 219–222, https://doi.org/10.1016/j.cirp.2013.03.031.

[9] A. Franco, L. Romoli, A. Musacchio, Modelling for predicting seam geometry in laser beam welding of stainless steel, Int. J. Therm. Sci. 79 (2014) 194–205, https://doi.org/10.1016/j.ijthermalsci.2014.01.003.

[10] J. Ning, D.E. Sievers, H. Garmestani, S.Y. Liang, Analytical modeling of in-process temperature in powder bed additive manufacturing considering laser power absorption, latent heat, scanning strategy, and powder packing, Materials 12 (5) (2019) 808, https://doi.org/10.3390/ma12050808.

[11] J. Li, Q. Wang, P. Michaleris, An analytical computation of temperature field evolved in directed energy deposition, J. Manuf. Sci. Eng. 140 (10) (2018) 101004, https://doi.org/10.1115/1.4040621.

[12] I. Yadroitsev, A. Gusarov, I. Yadroitsava, I. Smurov, Single track formation in selective laser melting of metal powders, J. Mater. Process. Technol. 210 (12) (2010) 1624–1631, https://doi.org/10.1016/j.jmatprotec.2010.05.010.

[13] E. Soderstrom, P. Mendez, Humping mechanisms present in high speed welding, Sci. Technol. Weld. Join. 11 (5) (2006) 572–579, https://doi.org/10.1179/174329306X120787.

[14] M. Moda, Modeling of powder bed fusion additive manufacturing, Ph.D. thesis, University of Pisa (2021), https://doi.org/10.13131/etd/03092021-124517.

[15] J.P. Oliveira, A.D. LaLonde, J. Ma, Processing parameters in laser powder bed fusion metal additive manufacturing, Mater. Des. 193 (2020) 108762, https://doi.org/10.1016/j.matdes.2020.108762.

[16] D.R. Clymer, J. Cagan, J. Beuth, Power-Velocity Process Design Charts for Powder Bed Additive Manufacturing, J. Mech. Des. 139 (10) (2017) 100907, https://doi.org/10.1115/1.4037302.

[17] A.A. Bhatti, Z. Barsoum, H. Murakawa, I. Barsoum, Influence of thermo-mechanical material properties of different steel grades on welding residual stresses and angular distortion, Mater. Des. 65 (2015) 878–889, https://doi.org/10.1016/j.matdes.2014.10.019.

[18] P. Asadi, S. Alimohammadi, O. Kohantorabi, A. Fazli, M. Akbari, Effects of material type, preheating and weld pass number on residual stress of welded steel pipes by multi-pass TIG welding (C-Mn, SUS304, SUS316), Therm. Sci. Eng. Prog. 16 (2020) 100462, https://doi.org/10.1016/j.tsep.2019.100462.

[19] C.Y. Wei, W. Jiang, Influence of welding groove on residual stress and distortion in T-joint weld, IOP Conf. Ser.: Mater. Sci. Eng. 733 (1) (2020) 012010, https://doi.org/10.1088/1757-899x/733/1/012010.

[20] J.H. Lee, B.S. Jang, H.J. Kim, S.H. Shim, S.W. Im, The effect of weld residual stress on fracture toughness at the intersection of two welding lines of offshore tubular structure, Mar. Struct. 71 (2020) 102708, https://doi.org/10.1016/j.marstruc.2020.102708.

[21] I.W. Bang, Y.P. Son, K.H. Oh, Y.P. Kim, W.S. Kim, Numerical simulation of sleeve repair welding of in-service gas pipelines, Weld. J. 81 (12) (2002) 273-S.

[22] G.S. Brar, Residual Stresses in Butt Welding of Two Circular Pipes: An Experimental and Numerical Investigation, Proceedings of the ASME 2014 Pressure Vessels and Piping Conference 1 (2014) V001T01A117, https://doi.org/10.1115/PVP2014-29082.

[23] X. Cai, B. Dong, S. Lin, A.B. Murphy, C. Fan, C. Yang, Heat source characteristics of ternary-gas-shielded tandem narrow-gap GMAW, Materials 12 (9) (2019) 1397, https://doi.org/10.3390/ma12091397.

[24] S.Y. Hwang, Y. Kim, J.H. Lee, Finite element analysis of residual stress distribution in a thick plate joined using two-pole tandem electro-gas welding, J. Mater. Process. Technol. 229 (2016) 349–360, https://doi.org/10.1016/j.jmatprotec.2015.09.037.

[25] J. Baumgartner, T. Bruder, Influence of weld geometry and residual stresses on the fatigue strength of longitudinal stiffeners, Weld. World 57 (6) (2013) 841–855, https://doi.org/10.1007/s40194-013-0078-7.

[26] A. Chiocca, F. Frendo, L. Bertini, Evaluation of Heat Sources for the Simulation of the Temperature Distribution in Gas Metal Arc Welded Joints, Metals 9 (11) (2019) 1142, https://doi.org/10.3390/met9111142.

[27] K. Hemmesi, P. Mallet, M. Farajian, Numerical evaluation of surface welding residual stress behavior under multiaxial mechanical loading and experimental validations, Int. J. Mech. Sci. 168 (2020) 105127, https://doi.org/10.1016/j.ijmecsci.2019.105127.

[28] J. Sun, J. Klassen, T. Nitschke-Pagel, K. Dilger, Effects of heat source geometric parameters and arc efficiency on welding temperature field, residual stress, and distortion in thin-plate full-penetration welds, Int. J. Adv. Manuf. Technol. 99 (1) (2018) 497–515, https://doi.org/10.1007/s00170-018-2516-6.

[29] F. Sikström, A.E. Öberg, Prediction of penetration in one-sided fillet welds by in-process joint gap monitoring–an experimental study, Weld. World 61 (3) (2017) 529–537, https://doi.org/10.1007/s40194-017-0448-7.

[30] H. Bang, H. Bang, C. Ro, S. Jeong, Mechanical Behavior of the Weld Joints of Thick Steel Plates Produced by Various Welding Processes, Strength Mater. 47 (1) (2015) 213–220, https://doi.org/10.1007/s11223-015-9650-2.

[31] J.C.F. Jorge, O.G. Meira, F.C.A. Madalena, L.F.G. de Souza, L.S. Araujo, M.C. Mendes, Evaluation of the AISI 904L Alloy Weld Overlays Obtained by GMAW and Electro-Slag Welding Processes, J. Mater. Eng. Perform. 26 (5) (2017) 2204–2212, https://doi.org/10.1007/s11665-017-2631-9.

[32] P. Colegrove, C. Ikeagu, A. Thistlethwaite, S. Williams, T. Nagy, W. Suder, A. Steuwer, T. Pirling, Welding process impact on residual stress and distortion, Sci. Technol. Weld. Join. 14 (8) (2009) 717–725, https://doi.org/10.1179/136217109X406938.

[33] C.M. Sonsino, T. Bruder, J. Baumgartner, S-N Lines for Welded Thin Joints – Suggested Slopes and FAT Values for Applying the Notch Stress Concept with Various Reference Radii, Weld. World 54 (11) (2010) R375–R392, https://doi.org/10.1007/BF03266752.

[34] C.M. Sonsino, M. Kueppers, M. Eibl, G. Zhang, Fatigue strength of laser beam welded thin steel structures under multiaxial loading, Int. J. Fatigue 28 (5–6) (2006) 657–662, https://doi.org/10.1016/j.ijfatigue.2005.09.013.

[35] S. Wu, Y. Shi, G. Zhang, S. Zhang, H. Liao, X. Wang, Z. Qin, Improving impact toughness of heavy section reduced activation ferritic martensitic CLF-1 steel joints with electron beam welding, J. Nucl. Mater. 531 (2020) 152031, https://doi.org/10.1016/j.jnucmat.2020.152031.

[36] A. Fayazi Khanigi, A. Farnia, M. Ardestani, M.J. Torkamany, Microstructure and mechanical properties of low power pulsed Nd:YAG laser welded S700MC steel, Sādhanā 45 (1) (2020) 54, https://doi.org/10.1007/s12046-020-1279-6.

[37] C.S. Kim, Thermophysical properties of stainless steels, Tech. Rep. ANL-75-55, Argonne National Laboratory (1975).

[38] H.J. Rack, Physical and Mechanical Properties of Cast 17-4 PH Stainless Steel, Tech. Rep. SAND-80-2302, OSTI (1981), https://doi.org/10.2172/6607517.

[39] P.W. Fuerschbach, G.R. Eisler, Determination of Material Properties for Welding Models by Means of Arc Weld Experiments, ASM Proceedings of the International Conference: Trends in Welding Research (2002) 782–786.

[40] B. Wilthan, H. Reschab, R. Tanzer, W. Schützenhöfer, G. Pottlacher, Thermophysical properties of a chromium-nickel-molybdenum steel in the solid and liquid phases, Int. J. Thermophys. 29 (1) (2008) 434–444, https://doi.org/10.1007/s10765-007-0300-1.

[41] J. Rahman Chukkan, M. Vasudevan, S. Muthukumaran, R. Ravi Kumar, N. Chandrasekhar, Simulation of laser butt welding of AISI 316L stainless steel sheet using various heat sources and experimental validation, J. Mater. Process. Technol. 219 (2015) 48–59, https://doi.org/10.1016/j.jmatprotec.2014.12.008.

[42] P. Pichler, B.J. Simonds, J.W. Sowards, G. Pottlacher, Measurements of thermophysical properties of solid and liquid NIST SRM 316L stainless steel, J. Mater. Sci. 55 (9) (2020) 4081–4093, https://doi.org/10.1007/s10853-019-04261-6.

[43] W.H. Dai, Y.T. Song, J.J. Xin, C. Fang, J. Wei, J.F. Wu, Numerical simulation of the ITER BTCC prototype case enclosure welding, Fusion Eng. Des. 154 (2020) 111538, https://doi.org/10.1016/j.fusengdes.2020.111538.

[44] D. Katherasan, P. Sathiya, A. Raja, Shielding gas effects on flux cored arc welding of AISI 316L (N) austenitic stainless steel joints, Mater. Des. 45 (2013) 43–51, https://doi.org/10.1016/j.matdes.2012.09.012.

[45] Y.N. Hu, S.C. Wu, Z.K. Wu, X.L. Zhong, S. Ahmed, S. Karabal, X.H. Xiao, H.O. Zhang, P.J. Withers, A new approach to correlate the defect population with the fatigue life of selective laser melted Ti-6Al-4V alloy, Int. J. Fatigue 136 (2020) 105584, https://doi.org/10.1016/j.ijfatigue.2020.105584.

[46] A. Das, R. Fritz, M. Finuf, I. Masters, Blue laser welding of multi-layered AISI 316L stainless steel micro-foils, Opt. Laser Technol. 132 (2020) 106498, https://doi.org/10.1016/j.optlastec.2020.106498.

[47] M.A. Melia, H.D.A. Nguyen, J.M. Rodelas, E.J. Schindelholz, Corrosion properties of 304L stainless steel made by directed energy deposition additive manufacturing, Corros. Sci. 152 (2019) 20–30, https://doi.org/10.1016/j.corsci.2019.02.029.

[48] M. Manjaiah, J.Y. Hascoët, M. Rauch, Effect of process parameters on track geometry, microstructural evolution on 316L stainless steel multi-layer clads, Mater. Sci. Eng. B 259 (2020) 114583, https://doi.org/10.1016/j.mseb.2020.114583.

[49] J. Nie, L. Wei, D. Li, L. Zhao, Y. Jiang, Q. Li, High-throughput characterization of microstructure and corrosion behavior of additively manufactured SS316L-SS431 graded material, Addit. Manuf. 35 (2020) 101295, https://doi.org/10.1016/j.addma.2020.101295.

[50] M. Rashkovets, M. Mazzarisi, A.A. Nikulina, G. Casalino, Analysis of laser direct stainless steel powder deposition on Ti6Al4V substrate, Mater. Lett. 274 (2020) 128064, https://doi.org/10.1016/j.matlet.2020.128064.

[51] Y. Su, B. Chen, C. Tan, X. Song, J. Feng, Influence of composition gradient variation on the microstructure and mechanical properties of 316 L/Inconel718 functionally graded material fabricated by laser additive manufacturing, J. Mater. Process. Technol. 283 (2020) 116702, https://doi.org/10.1016/j.jmatprotec.2020.116702.

[52] E. Azinpour, R. Darabi, J. Cesar de Sa, A. Santos, J. Hodek, J. Dzugan, Fracture analysis in directed energy deposition (DED) manufactured 316L stainless steel using a phase-field approach, Finite Elem. Anal. Des. 177 (2020) 103417, https://doi.org/10.1016/j.finel.2020.103417.

[53] Z. Yu, Y. Zheng, J. Chen, C. Wu, J. Xu, H. Lu, C. Yu, Effect of laser remelting processing on microstructure and mechanical properties of 17–4 PH stainless steel during laser direct metal deposition, J. Mater. Process. Technol. 284 (2020) 116738, https://doi.org/10.1016/j.jmatprotec.2020.116738.

[54] Y. Yang, Y. Gong, S. Qu, B. Xin, Y. Xu, Y. Qi, Additive/subtractive hybrid manufacturing of 316L stainless steel powder: Densification, microhardness and residual stress, J. Mech. Sci. Technol. 33 (12) (2019) 5797–5807, https://doi.org/10.1007/s12206-019-1126-z.
[55] F. Pöhl, C. Hardes, F. Scholz, J. Frenzel, Orientation-dependent deformation behavior of 316L steel manufactured by laser metal deposition and casting under local scratch and indentation load, Materials 13 (7) (2020) 1765, https://doi.org/10.3390/MA13071765.
[56] D.R. Feenstra, A. Molotnikov, N. Birbilis, Effect of energy density on the interface evolution of stainless steel 316L deposited upon INC 625 via directed energy deposition, J. Mater. Sci. 55 (27) (2020) 13314–13328, https://doi.org/10.1007/s10853-020-04913-y.
[57] R.I. Revilla, M. Van Calster, M. Raes, G. Arroud, F. Andreatta, L. Pyl, P. Guillaume, I. De Graeve, Microstructure and corrosion behavior of 316L stainless steel prepared using different additive manufacturing methods: A comparative study bringing insights into the impact of microstructure on their passivity, Corros. Sci. 176 (2020) 108914, https://doi.org/10.1016/j.corsci.2020.108914.
[58] Z. Sun, X. Tan, S.B. Tor, W.Y. Yeong, Selective laser melting of stainless steel 316L with low porosity and high build rates, Mater. Des. 104 (2016) 197–204, https://doi.org/10.1016/j.matdes.2016.05.035.
[59] J.C. Simmons, X. Chen, A. Azizi, M.A. Daeumer, P.Y. Zavalij, G. Zhou, S.N. Schiffres, Influence of processing and microstructure on the local and bulk thermal conductivity of selective laser melted 316L stainless steel, Addit. Manuf. 32 (2020) 100996, https://doi.org/10.1016/j.addma.2019.100996.
[60] E. Tascioglu, Y. Karabulut, Y. Kaynak, Correction to: Influence of heat treatment temperature on the microstructural, mechanical, and wear behavior of 316L stainless steel fabricated by laser powder bed additive manufacturing, Int. J. Adv. Manuf. Technol. 107 (5) (2020) 1957, https://doi.org/10.1007/s00170-020-05115-1.
[61] J. Yan, Y. Zhou, R. Gu, X. Zhang, W.M. Quach, M. Yan, A comprehensive study of steel powders (316L, H13, P20 and 18Ni300) for their selective laser melting additive manufacturing, Metals 9 (1) (2019) 86, https://doi.org/10.3390/met9010086.
[62] H. Gu, H. Gong, D. Pal, K. Rafi, T. Starr, B. Stucker, Influences of Energy Density on Porosity and Microstructure of Selective Laser Melted 17–4PH Stainless Steel, 24th International Solid Freeform Fabrication Symposium (2013) 474–489, https://doi.org/10.26153/tsw/15572.
[63] Z. Hu, H. Zhu, H. Zhang, X. Zeng, Experimental investigation on selective laser melting of 17–4PH stainless steel, Opt. Laser Technol. 87 (2017) 17–25, https://doi.org/10.1016/j.optlastec.2016.07.012.
[64] P.D. Nezhadfar, E. Burford, K. Anderson-Wedge, B. Zhang, S. Shao, S.R. Daniewicz, N. Shamsaei, Fatigue crack growth behavior of additively manufactured 17–4 PH stainless steel: Effects of build orientation and microstructure, Int. J. Fatigue 123 (2019) 168–179, https://doi.org/10.1016/j.ijfatigue.2019.02.015.
[65] X. Wang, L. Zhao, J.Y.H. Fuh, H.P. Lee, Experimental characterization and micromechanical-statistical modeling of 316L stainless steel processed by selective laser melting, Comput. Mater. Sci. 177 (2020) 109595, https://doi.org/10.1016/j.commatsci.2020.109595.
[66] C. Wei, Z. Sun, Y. Huang, L. Li, Embedding anti-counterfeiting features in metallic components via multiple material additive manufacturing, Addit. Manuf. 24 (2018) 1–12, https://doi.org/10.1016/j.addma.2018.09.003.
[67] Z. Zhu, W. Li, Q.B. Nguyen, X. An, W. Lu, Z. Li, F.L. Ng, S.M. Ling Nai, J. Wei, Enhanced strength–ductility synergy and transformation-induced plasticity of the selective laser melting fabricated 304L stainless steel, Addit. Manuf. 35 (2020) 101300, https://doi.org/10.1016/j.addma.2020.101300.
[68] P. Bian, J. Shi, Y. Liu, Y. Xie, Influence of laser power and scanning strategy on residual stress distribution in additively manufactured 316L steel, Opt. Laser Technol. 132 (2020) 106477, https://doi.org/10.1016/j.optlastec.2020.106477.
[69] E. Liverani, S. Toschi, L. Ceschini, A. Fortunato, Effect of selective laser melting (SLM) process parameters on microstructure and mechanical properties of 316L austenitic stainless steel, J. Mater. Process. Technol. 249 (2017) 255–263, https://doi.org/10.1016/j.jmatprotec.2017.05.042.
[70] J. Zhao, J. Hou, L. Chen, B. Dai, X. Xiong, L. Tan, K. Zhang, A. Huang, Evaluating impact performance of a selective laser melted 304L stainless steel with weak texture, Mater. Today Commun. 25 (2020) 101299, https://doi.org/10.1016/j.mtcomm.2020.101299.
[71] V. Cruz, Q. Chao, N. Birbilis, D. Fabijanic, P.D. Hodgson, S. Thomas, Electrochemical studies on the effect of residual stress on the corrosion of 316L manufactured by selective laser melting, Corros. Sci. 164 (2020) 108314, https://doi.org/10.1016/j.corsci.2019.108314.
[72] J. Hou, W. Chen, Z. Chen, K. Zhang, A. Huang, Microstructure, tensile properties and mechanical anisotropy of selective laser melted 304L stainless steel, J. Mater. Sci. Technol. 48 (2020) 63–71, https://doi.org/10.1016/j.jmst.2020.01.011.
[73] S. Alvi, K. Saeidi, F. Akhtar, High temperature tribology and wear of selective laser melted (SLM) 316L stainless steel, Wear 448–449 (2020) 203228, https://doi.org/10.1016/j.wear.2020.203228.
[74] Y. Bai, C. Zhao, J. Yang, J.Y.H. Fuh, W.F. Lu, C. Weng, H. Wang, Dry mechanical-electrochemical polishing of selective laser melted 316L stainless steel, Mater. Des. 193 (2020) 108840, https://doi.org/10.1016/j.matdes.2020.108840.
[75] A.B. Kale, B.K. Kim, D.I. Kim, E.G. Castle, M. Reece, S.H. Choi, An investigation of the corrosion behavior of 316L stainless steel fabricated by SLM and SPS techniques, Mater. Charact. 163 (2020) 110204, https://doi.org/10.1016/j.matchar.2020.110204.
[76] J. Džugan, K. Halmešová, M. Ackermann, M. Koukolíková, Z. Trojanová, Thermo-physical properties investigation in relation to deposition orientation for SLM deposited H13 steel, Thermochim. Acta 683 (2020) 178479, https://doi.org/10.1016/j.tca.2019.178479.
[77] J. Zhu, M. Khurshid, Z. Barsoum, Accuracy of computational welding mechanics methods for estimation of angular distortion and residual stresses, Weld. World 63 (5) (2019) 1391–1405, https://doi.org/10.1007/s40194-019-00746-9.
[78] D.S. Shim, G.Y. Baek, J.S. Seo, G.Y. Shin, K.P. Kim, K.Y. Lee, Effect of layer thickness setting on deposition characteristics in direct energy deposition (DED) process, Opt. Laser Technol. 86 (2016) 69–78, https://doi.org/10.1016/j.optlastec.2016.07.001.
[79] M. Åsberg, G. Fredriksson, S. Hatami, W. Fredriksson, P. Krakhmalev, Influence of post treatment on microstructure, porosity and mechanical properties of additive manufactured H13 tool steel, Mater. Sci. Eng. A 742 (2019) 584–589, https://doi.org/10.1016/j.msea.2018.08.046.
[80] J.J. Yan, D.L. Zheng, H.X. Li, X. Jia, J.F. Sun, Y.L. Li, M. Qian, M. Yan, Selective laser melting of H13: microstructure and residual stress, J. Mater. Sci. 52 (20) (2017) 12476–12485, https://doi.org/10.1007/s10853-017-1380-3.
[81] M. Wang, W. Li, Y. Wu, S. Li, C. Cai, S. Wen, Q. Wei, Y. Shi, F. Ye, Z. Chen, High-Temperature Properties and Microstructural Stability of the AISI H13 Hot-Work Tool Steel Processed by Selective Laser Melting, Metall. Mater. Trans. B 50 (1) (2019) 531–542, https://doi.org/10.1007/s11663-018-1442-1.
[82] J. Yan, H. Song, Y. Dong, W.M. Quach, M. Yan, High strength (~2000 MPa) or highly ductile (~11%) additively manufactured H13 by tempering at different conditions, Mater. Sci. Eng. A 773 (2020) 138845, https://doi.org/10.1016/j.msea.2019.138845.
[83] F. Hengsbach, P. Koppa, M.J. Holzweissig, M.E. Aydinöz, A. Taube, K.P. Hoyer, O. Starykov, B. Tonn, T. Niendorf, T. Tröster, M. Schaper, Inline additively manufactured functionally graded multi-materials: microstructural and mechanical characterization of 316L parts with H13 layers, Prog. Addit. Manuf. 3 (4) (2018) 221–231, https://doi.org/10.1007/s40964-018-0044-4.
[84] B. Ren, D. Lu, R. Zhou, Z. Li, J. Guan, Preparation and mechanical properties of selective laser melted H13 steel, J. Mater. Res. 34 (8) (2019) 1415–1425, https://doi.org/10.1557/jmr.2019.10.
[85] M. Narvan, K.S. Al-Rubaie, M. Elbestawi, Process-structure-property relationships of AISI H13 tool steel processed with selective laser melting, Materials 12 (14) (2019) 2284, https://doi.org/10.3390/ma12142284.
[86] M. Wang, Y. Wu, Q. Wei, Y. Shi, Thermal fatigue properties of H13 hot-work tool steels processed by selective laser melting, Metals 10 (1) (2020) 116, https://doi.org/10.3390/met10010116.
[87] P.J. Raboin, The mechanical behavior of maraging steel under extreme electromechanical and thermal conditions, Ph.D. thesis, Massachusetts Institute of Technology (1989).
[88] E. Yasa, K. Kempen, J.P. Kruth, L. Thijs, J. Van Humbeeck, Microstructure and mechanical properties of maraging steel 300 after selective laser melting, 21st International Solid Freeform Fabrication Symposium (2010) 383–396, https://doi.org/10.26153/tsw/15205.
[89] Y. Bai, Y. Yang, D. Wang, M. Zhang, Influence mechanism of parameters process and mechanical properties evolution mechanism of maraging steel 300 by selective laser melting, Mater. Sci. Eng. A 703 (2017) 116–123, https://doi.org/10.1016/j.msea.2017.06.033.
[90] J. Damon, T. Hanemann, S. Dietrich, G. Graf, K.H. Lang, V. Schulze, Orientation dependent fatigue performance and mechanisms of selective laser melted maraging steel X3NiCoMoTi18-9-5, Int. J. Fatigue 127 (2019) 395–402, https://doi.org/10.1016/j.ijfatigue.2019.06.025.
[91] L. Mugwagwa, I. Yadroitsev, S. Matope, Effect of Process Parameters on Residual Stresses, Distortions, and Porosity in Selective Laser Melting of Maraging Steel 300, Metals 9 (10) (2019) 1042, https://doi.org/10.3390/met9101042.
[92] T. Bhardwaj, M. Shukla, Effect of scan direction on tensile properties and fractography of laser additive manufactured maraging steel, Mater. Today: Proc. 18 (2019) 3842–3848, https://doi.org/10.1016/j.matpr.2019.07.323.
[93] J. Mutua, S. Nakata, T. Onda, Z.C. Chen, Optimization of selective laser melting parameters and influence of post heat treatment on microstructure and mechanical properties of maraging steel, Mater. Des. 139 (2018) 486–497, https://doi.org/10.1016/j.matdes.2017.11.042.
[94] M. Zhang, Y. Yang, D. Wang, C. Song, J. Chen, Microstructure and mechanical properties of CuSn/18Ni300 bimetallic porous structures manufactured by selective laser melting, Mater. Des. 165 (2019) 107583, https://doi.org/10.1016/j.matdes.2019.107583.
[95] S. Shakerin, A. Hadadzadeh, B.S. Amirkhiz, S. Shamsdini, J. Li, M. Mohammadi, Additive manufacturing of maraging steel-H13 bimetals using laser powder bed fusion technique, Addit. Manuf. 29 (2019) 100797, https://doi.org/10.1016/j.addma.2019.100797.
[96] Z. Lei, S. Wu, P. Li, B. Li, N. Lu, X. Hu, Numerical study of thermal fluid dynamics in laser welding of Al alloy with powder feeding, Appl. Therm. Eng. 151 (2019) 394–405, https://doi.org/10.1016/j.applthermaleng.2019.02.040.
[97] Z. Lei, S. Wu, B. Cao, B. Li, J. Liang, X. Hu, Y. Chen, Role of thermal fluid dynamics in alloying element distribution and weld porosity in powder feeding-based laser welding of Al alloy, Appl. Therm. Eng. 171 (2020) 115081, https://doi.org/10.1016/j.applthermaleng.2020.115081.
[98] S. Chen, Y. Wu, Y. Li, M. Chen, Q. Zheng, X. Zhan, Study on 2219 Al-Cu alloy T-joint used dual laser beam bilateral synchronous welding: Parameters

optimization based on the simulation of temperature field and residual stress, Opt. Laser Technol. 132 (2020) 106481, https://doi.org/10.1016/j.optlastec.2020.106481.
[99] Y. Zhao, X. Zhan, S. Chen, M. Bai, X. Gong, Study on the shear performance and fracture mechanism of T-joints for 2219 aluminum alloy by dual laser-beam bilateral synchronous welding, J. Alloy. Compd. 847 (2020) 156511, https://doi.org/10.1016/j.jallcom.2020.156511.
[100] J. Ahn, E. He, L. Chen, T. Pirling, J.P. Dear, C.M. Davies, Determination of residual stresses in fibre laser welded AA2024-T3 T-joints by numerical simulation and neutron diffraction, Mater. Sci. Eng. A 712 (2018) 685–703, https://doi.org/10.1016/j.msea.2017.12.027.
[101] J. Enz, S. Riekehr, V. Ventzke, N. Kashaev, Influence of the Local Chemical Composition on the Mechanical Properties of Laser Beam Welded Al-Li Alloys, Phys. Procedia 39 (2012) 51–58, https://doi.org/10.1016/j.phpro.2012.10.013.
[102] B. Han, Y. Chen, W. Tao, H. Li, L. Li, Microstructural evolution and interfacial crack corrosion behavior of double-sided laser beam welded 2060/2099 Al-Li alloys T-joints, Mater. Des. 135 (2017) 353–365, https://doi.org/10.1016/j.matdes.2017.09.042.
[103] T. Gu, B. Chen, C. Tan, J. Feng, Microstructure evolution and mechanical properties of laser additive manufacturing of high strength Al-Cu-Mg alloy, Opt. Laser Technol. 112 (2019) 140–150, https://doi.org/10.1016/j.optlastec.2018.11.008.
[104] H. Zhang, H. Zhu, X. Nie, J. Yin, Z. Hu, X. Zeng, Effect of Zirconium addition on crack, microstructure and mechanical behavior of selective laser melted Al-Cu-Mg alloy, Scripta Mater. 134 (2017) 6–10, https://doi.org/10.1016/j.scriptamat.2017.02.036.
[105] Q. Tan, Y. Liu, Z. Fan, J. Zhang, Y. Yin, M.X. Zhang, Effect of processing parameters on the densification of an additively manufactured 2024 Al alloy, J. Mater. Sci. Technol. 58 (2020) 34–45, https://doi.org/10.1016/j.jmst.2020.03.070.
[106] P. Yang, L.A. Deibler, D.R. Bradley, D.K. Stefan, J.D. Carroll, Microstructure evolution and thermal properties of an additively manufactured, solution treatable AlSi10Mg part, J. Mater. Res. 33 (23) (2018) 4040–4052, https://doi.org/10.1557/jmr.2018.405.
[107] R. Sepe, J. Wiebesiek, C.M. Sonsino, Numerical and experimental validation of residual stresses of laser-welded joints and their influence on the fatigue behaviour, Fatigue Fract. Eng. Mater. Struct. 43 (6) (2020) 1126–1141, https://doi.org/10.1111/ffe.13180.
[108] B. Möller, K. Schnabel, R. Wagener, H. Kaufmann, T. Melz, Fatigue assessment of additively manufactured AlSi10Mg laser beam welded to rolled EN AW-6082-T6 sheet metal, Int. J. Fatigue 140 (2020) 105805, https://doi.org/10.1016/j.ijfatigue.2020.105805.
[109] N. Read, W. Wang, K. Essa, M.M. Attallah, Selective laser melting of AlSi10Mg alloy: Process optimisation and mechanical properties development, Mater. Des. 65 (2015) 417–424, https://doi.org/10.1016/j.matdes.2014.09.044.
[110] R. Casati, M. Hamidi Nasab, M. Coduri, V. Tirelli, M. Vedani, Effects of Platform Pre-Heating and Thermal-Treatment Strategies on Properties of AlSi10Mg Alloy Processed by Selective Laser Melting, Metals 8 (11) (2018) 954, https://doi.org/10.3390/met8110954.
[111] A. Tridello, J. Fiocchi, C.A. Biffi, G. Chiandussi, M. Rossetto, A. Tuissi, D.S. Paolino, VHCF response of Gaussian SLM AlSi10Mg specimens: Effect of a stress relief heat treatment, Int. J. Fatigue 124 (2019) 435–443, https://doi.org/10.1016/j.ijfatigue.2019.02.020.
[112] I. Maskery, N.T. Aboulkhair, A.O. Aremu, C.J. Tuck, I.A. Ashcroft, R.D. Wildman, R.J.M. Hague, A mechanical property evaluation of graded density Al-Si10-Mg lattice structures manufactured by selective laser melting, Mater. Sci. Eng. A 670 (2016) 264–274, https://doi.org/10.1016/j.msea.2016.06.013.
[113] A.H. Maamoun, Y.F. Xue, M.A. Elbestawi, S.C. Veldhuis, Effect of Selective Laser Melting Process Parameters on the Quality of Al Alloy Parts: Powder Characterization, Density, Surface Roughness, and Dimensional Accuracy, Materials 11 (12) (2018) 2343, https://doi.org/10.3390/ma11122343.
[114] L. Hitzler, S. Hafenstein, F. Mendez Martin, H. Clemens, E. Sert, A. Öchsner, M. Merkel, E. Werner, Heat treatments and critical quenching rates in additively manufactured Al-Si-Mg alloys, Materials 13 (3) (2020) 720, https://doi.org/10.3390/ma13030720.
[115] A. Hadadzadeh, B.S. Amirkhiz, S. Shakerin, J. Kelly, J. Li, M. Mohammadi, Microstructural investigation and mechanical behavior of a two-material component fabricated through selective laser melting of AlSi10Mg on an Al-Cu-Ni-Fe-Mg cast alloy substrate, Addit. Manuf. 31 (2020) 100937, https://doi.org/10.1016/j.addma.2019.100937.
[116] Z. Li, Y. Nie, B. Liu, Z. Kuai, M. Zhao, F. Liu, Mechanical properties of AlSi10Mg lattice structures fabricated by selective laser melting, Mater. Des. 192 (2020) 108709, https://doi.org/10.1016/j.matdes.2020.108709.
[117] P. Ferro, A. Fabrizi, F. Berto, G. Savio, R. Meneghello, S. Rosso, Defects as a root cause of fatigue weakening of additively manufactured AlSi10Mg components, Theoret. Appl. Fract. Mech. 108 (2020) 102611, https://doi.org/10.1016/j.tafmec.2020.102611.
[118] E. Padovano, C. Badini, A. Pantarelli, F. Gili, F. D'Aiuto, A comparative study of the effects of thermal treatments on AlSi10Mg produced by laser powder bed fusion, J. Alloy. Compd. 831 (2020) 154822, https://doi.org/10.1016/j.jallcom.2020.154822.
[119] T. Hirata, T. Kimura, T. Nakamoto, Effects of hot isostatic pressing and internal porosity on the performance of selective laser melted AlSi10Mg alloys, Mater. Sci. Eng. A 772 (2020) 138713, https://doi.org/10.1016/j.msea.2019.138713.
[120] L.F. Wang, J. Sun, X.L. Yu, Y. Shi, X.G. Zhu, L.Y. Cheng, H.H. Liang, B. Yan, L.J. Guo, Enhancement in mechanical properties of selectively laser-melted AlSi10Mg aluminum alloys by T6-like heat treatment, Mater. Sci. Eng. A 734 (2018) 299–310, https://doi.org/10.1016/j.msea.2018.07.103.
[121] T. Kimura, T. Nakamoto, Microstructures and mechanical properties of A356 (AlSi7Mg0.3) aluminum alloy fabricated by selective laser melting, Mater. Des. 89 (2016) 1294–1301, https://doi.org/10.1016/j.matdes.2015.10.065.
[122] H. Rao, S. Giet, K. Yang, X. Wu, C.H.J. Davies, The influence of processing parameters on aluminium alloy A357 manufactured by Selective Laser Melting, Mater. Des. 109 (2016) 334–346, https://doi.org/10.1016/j.matdes.2016.07.009.
[123] J.H. Rao, Y. Zhang, K. Zhang, X. Wu, A. Huang, Selective laser melted Al-7Si-0.6Mg alloy with in-situ precipitation via platform heating for residual strain removal, Mater. Des. 182 (2019) 108005, https://doi.org/10.1016/j.matdes.2019.108005.
[124] APWorks, Material Data Sheet - Scalmalloy (2017).
[125] X.K. Zhu, Y.J. Chao, Effects of temperature-dependent material properties on welding simulation, Comput. Struct. 80 (11) (2002) 967–976, https://doi.org/10.1016/S0045-7949(02)00040-8.
[126] N. Contuzzi, S.L. Campanelli, G. Casalino, A.D. Ludovico, On the role of the Thermal Contact Conductance during the Friction Stir Welding of an AA5754-H111 butt joint, Appl. Therm. Eng. 104 (2016) 263–273, https://doi.org/10.1016/j.applthermaleng.2016.05.071.
[127] W. Tao, S. Yang, Weld zone porosity elimination process in remote laser welding of AA5182-O aluminum alloy lap-joints, J. Mater. Process. Technol. 286 (2020) 116826, https://doi.org/10.1016/j.jmatprotec.2020.116826.
[128] F. Liu, C. Tan, L. Wu, X. Gong, B. Chen, X. Song, H. Zhao, G. Wang, Influence of waveforms on Laser-MIG hybrid welding characteristics of 5052 aluminum alloy assisted by magnetic field, Opt. Laser Technol. 132 (2020) 106508, https://doi.org/10.1016/j.optlastec.2020.106508.
[129] P. Kürnsteiner, P. Bajaj, A. Gupta, M.B. Wilms, A. Weisheit, X. Li, C. Leinenbach, B. Gault, E.A. Jägle, D. Raabe, Control of thermally stable core-shell nano-precipitates in additively manufactured Al-Sc-Zr alloys, Addit. Manuf. 32 (2020) 100910, https://doi.org/10.1016/j.addma.2019.100910.
[130] M. Froend, V. Ventzke, N. Kashaev, B. Klusemann, J. Enz, Thermal analysis of wire-based direct energy deposition of Al-Mg using different laser irradiances, Addit. Manuf. 29 (2019) 100800, https://doi.org/10.1016/j.addma.2019.100800.
[131] R. Li, H. Chen, H. Zhu, M. Wang, C. Chen, T. Yuan, Effect of aging treatment on the microstructure and mechanical properties of Al-3.02Mg-0.2Sc-0.1Zr alloy printed by selective laser melting, Mater. Des. 168 (2019) 107668, https://doi.org/10.1016/j.matdes.2019.107668.
[132] Q. Jia, P. Rometsch, P. Kürnsteiner, Q. Chao, A. Huang, M. Weyland, L. Bourgeois, X. Wu, Selective laser melting of a high strength Al-Mn-Sc alloy: Alloy design and strengthening mechanisms, Acta Mater. 171 (2019) 108–118, https://doi.org/10.1016/j.actamat.2019.04.014.
[133] A.B. Spierings, K. Dawson, K. Kern, F. Palm, K. Wegener, SLM-processed Sc- and Zr- modified Al-Mg alloy: Mechanical properties and microstructural effects of heat treatment, Mater. Sci. Eng. A 701 (2017) 264–273, https://doi.org/10.1016/j.msea.2017.06.089.
[134] Y. Shi, P. Rometsch, K. Yang, F. Palm, X. Wu, Characterisation of a novel Sc and Zr modified Al–Mg alloy fabricated by selective laser melting, Mater. Lett. 196 (2017) 347–350, https://doi.org/10.1016/j.matlet.2017.03.089.
[135] J.P. Best, X. Maeder, J. Michler, A.B. Spierings, Mechanical Anisotropy Investigated in the Complex SLM-Processed Sc- and Zr-Modified Al–Mg Alloy Microstructure, Adv. Eng. Mater. 21 (3) (2019) 1801113, https://doi.org/10.1002/adem.201801113.
[136] J. Bi, Z. Lei, Y. Chen, X. Chen, Z. Tian, X. Qin, J. Liang, X. Zhang, Effect of Al3(Sc, Zr) and Mg2Si precipitates on microstructure and tensile properties of selective laser melted Al-14.1Mg-0.47Si-0.31Sc-0.17Zr alloy, Intermetallics 123 (2020) 106822, https://doi.org/10.1016/j.intermet.2020.106822.
[137] D. Koutny, D. Skulina, L. Pantělejev, D. Paloušek, B. Lenczowski, F. Palm, A. Nick, Processing of Al-Sc aluminum alloy using SLM technology, Procedia CIRP 74 (2018) 44–48, https://doi.org/10.1016/j.procir.2018.08.027.
[138] H. Atharifar, D. Lin, R. Kovacevic, Numerical and experimental investigations on the loads carried by the tool during friction stir welding, J. Mater. Eng. Perform. 18 (4) (2009) 339–350, https://doi.org/10.1007/s11665-008-9298-1.
[139] R. Kumar, U. Dilthey, D.K. Dwivedi, S.P. Sharma, P.K. Ghosh, Welding of thin sheet of Al alloy (6082) by using Vario wire DC P-GMAW, Int. J. Adv. Manuf. Technol. 42 (1) (2009) 102, https://doi.org/10.1007/s00170-008-1568-4.
[140] C. Xu, K. Liu, H. He, H. Xiang, X. Zhang, L. Li, Mechanical Performance Evaluation of the Al-Mg-Si-(Cu) Aluminum Alloys after Transient Thermal Shock through an Novel Equivalent Structure Design and Finite Element Modeling, Metals 10 (4) (2020) 537, https://doi.org/10.3390/met10040537.
[141] R.H.M. de Siqueira, A.C. de Oliveira, R. Riva, A.J. Abdalla, C.A.R.P. Baptista, M.S. F. de Lima, Mechanical and microstructural characterization of laser-welded joints of 6013-T4 aluminum alloy, J. Braz. Soc. Mech. Sci. Eng. 37 (1) (2015) 133–140, https://doi.org/10.1007/s40430-014-0175-6.
[142] A.C. Oliveira, R.H.M. Siqueira, R. Riva, M.S.F. Lima, One-sided laser beam welding of autogenous T-joints for 6013–T4 aluminium alloy, Mater. Des. 65 (2015) 726–736, https://doi.org/10.1016/j.matdes.2014.09.055.
[143] Z.B. Yang, W. Tao, L.Q. Li, Y.B. Chen, F.Z. Li, Y.L. Zhang, Double-sided laser beam welded T-joints for aluminum aircraft fuselage panels: Process, microstructure, and mechanical properties, Mater. Des. 33 (2012) 652–658, https://doi.org/10.1016/j.matdes.2011.07.059.

[144] Z. Yang, X. Zhao, W. Tao, C. Jin, S. Huang, Y. Wang, E. Zhang, Comparative study on successive and simultaneous double-sided laser beam welding of AA6056/AA6156 aluminum alloy T-joints for aircraft fuselage panels, Int. J. Adv. Manuf. Technol. 97 (1) (2018) 845–856, https://doi.org/10.1007/s00170-018-1996-8.
[145] W. Tao, Z. Yang, C. Shi, D. Dong, Simulating effects of welding speed on melt flow and porosity formation during double-sided laser beam welding of AA6056-T4/AA6156-T6 aluminum alloy T-joint, J. Alloy. Compd. 699 (2017) 638–647, https://doi.org/10.1016/j.jallcom.2016.12.371.
[146] Z. Yang, X. Zhao, W. Tao, C. Jin, Effects of keyhole status on melt flow and flow-induced porosity formation during double-sided laser welding of AA6056/AA6156 aluminium alloy T-joint, Opt. Laser Technol. 109 (2019) 39–48, https://doi.org/10.1016/j.optlastec.2018.07.065.
[147] W. Xiao, B. Wang, K. Zheng, J. Zhou, J. Lin, A study of interfacial heat transfer and its effect on quenching when hot stamping AA7075, Arch. Civ. Mech. Eng. 18 (3) (2018) 723–730, https://doi.org/10.1016/j.acme.2017.12.001.
[148] Y. Lu, S. Zhu, Z. Zhao, T. Chen, J. Zeng, Numerical simulation of residual stresses in aluminum alloy welded joints, J. Manuf. Process. 50 (2020) 380–393, https://doi.org/10.1016/j.jmapro.2019.12.056.
[149] D. Yan, X. Liu, J. Li, J. Yang, H. Fang, Effect of strain hardening and strain softening on welding distortion and residual stress of A7N01-T4 aluminum alloy by simulation analysis, J. Cent. South Univ. Technol. 17 (4) (2010) 666–673, https://doi.org/10.1007/s11771-010-0538-9.
[150] A. Langebeck, A. Bohlen, H. Freisse, F. Vollertsen, Additive manufacturing with the lightweight material aluminium alloy EN AW-7075, Weld. World 64 (3) (2020) 429–436, https://doi.org/10.1007/s40194-019-00831-z.
[151] Y. Otani, S. Sasaki, Effects of the addition of silicon to 7075 aluminum alloy on microstructure, mechanical properties, and selective laser melting processability, Mater. Sci. Eng. A 777 (2020) 139079, https://doi.org/10.1016/j.msea.2020.139079.
[152] Z. Lei, J. Bi, Y. Chen, X. Chen, X. Qin, Z. Tian, Effect of energy density on formability, microstructure and micro-hardness of selective laser melted Sc- and Zr- modified 7075 aluminum alloy, Powder Technol. 356 (2019) 594–606, https://doi.org/10.1016/j.powtec.2019.08.082.
[153] R. Casati, M. Coduri, M. Riccio, A. Rizzi, M. Vedani, Development of a high strength Al–Zn–Si–Mg–Cu alloy for selective laser melting, J. Alloy. Compd. 801 (2019) 243–253, https://doi.org/10.1016/j.jallcom.2019.06.123.
[154] C.H. Fu, Y.B. Guo, Three-Dimensional Temperature Gradient Mechanism in Selective Laser Melting of Ti-6Al-4V, J. Manuf. Sci. Eng. 136 (6) (2014) 061004, https://doi.org/10.1115/1.4028539.
[155] J. Lin, N. Ma, X. Liu, Y. Lei, Modification of residual stress distribution in welded joint of titanium alloy with multi electron beam heating, J. Mater. Process. Technol. 278 (2020) 116504, https://doi.org/10.1016/j.jmatprotec.2019.116504.
[156] K. Kumar, M. Masanta, S. Kumar Sahoo, Microstructure evolution and metallurgical characteristic of bead-on-plate TIG welding of Ti-6Al-4V alloy, J. Mater. Process. Technol. 265 (2019) 34–43, https://doi.org/10.1016/j.jmatprotec.2018.10.002.
[157] R. Reda, M. Magdy, M. Rady, Ti–6Al–4V TIG Weld Analysis Using FEM Simulation and Experimental Characterization, Iran. J. Sci. Technol. Trans. Mech. Eng. 44 (3) (2020) 765–782, https://doi.org/10.1007/s40997-019-00287-y.
[158] Y. Lu, R. Turner, J. Brooks, H. Basoalto, Microstructural characteristics and computational investigation on electron beam welded Ti-6Al-4 V alloy, J. Mater. Process. Technol. 288 (2021) 116837, https://doi.org/10.1016/j.jmatprotec.2020.116837.
[159] C. Churiaque, M.R. Amaya-Vazquez, F.J. Botana, J.M. Sánchez-Amaya, FEM Simulation and Experimental Validation of LBW Under Conduction Regime of Ti6Al4V Alloy, J. Mater. Eng. Perform. 25 (8) (2016) 3260–3269, https://doi.org/10.1007/s11665-016-2214-1.
[160] Q. Yunlian, D. Ju, H. Quan, Z. Liying, Electron beam welding, laser beam welding and gas tungsten arc welding of titanium sheet, Mater. Sci. Eng. A 280 (1) (2000) 177–181, https://doi.org/10.1016/S0921-5093(99)00662-0.
[161] Z. Li, S.L. Gobbi, I. Norris, S. Zolotovsky, K.H. Richter, Laser welding techniques for titanium alloy sheet, J. Mater. Process. Technol. 65 (1–3) (1997) 203–208, https://doi.org/10.1016/S0924-0136(96)02263-7.
[162] E. Akman, A. Demir, T. Canel, T. Sınmazçelik, Laser welding of Ti6Al4V titanium alloys, J. Mater. Process. Technol. 209 (8) (2009) 3705–3713, https://doi.org/10.1016/j.jmatprotec.2008.08.026.
[163] F. Caiazzo, V. Alfieri, G. Corrado, F. Cardaropoli, V. Sergi, Investigation and Optimization of Laser Welding of Ti-6Al-4 V Titanium Alloy Plates, J. Manuf. Sci. Eng. 135 (6) (2013) 061012, https://doi.org/10.1115/1.4025578.
[164] J. Yu, M. Rombouts, G. Maes, F. Motmans, Material Properties of Ti6Al4 V Parts Produced by Laser Metal Deposition, Phys. Procedia 39 (2012) 416–424, https://doi.org/10.1016/j.phpro.2012.10.056.
[165] M.N. Ahsan, A.J. Pinkerton, R.J. Moat, J. Shackleton, A comparative study of laser direct metal deposition characteristics using gas and plasma-atomized Ti-6Al-4V powders, Mater. Sci. Eng. A 528 (25–26) (2011) 7648–7657, https://doi.org/10.1016/j.msea.2011.06.074.
[166] B. Baufeld, E. Brandl, O. van der Biest, Wire based additive layer manufacturing: Comparison of microstructure and mechanical properties of Ti-6Al-4V components fabricated by laser-beam deposition and shaped metal deposition, J. Mater. Process. Technol. 211 (6) (2011) 1146–1158, https://doi.org/10.1016/j.jmatprotec.2011.01.018.
[167] S. Wolff, T. Lee, E. Faierson, K. Ehmann, J. Cao, Anisotropic properties of directed energy deposition (DED)-processed Ti-6Al-4V, J. Manuf. Process. 24 (2016) 397–405, https://doi.org/10.1016/j.jmapro.2016.06.020.
[168] J.C. Heigel, P. Michaleris, E.W. Reutzel, Thermo-mechanical model development and validation of directed energy deposition additive manufacturing of Ti-6Al-4V, Addit. Manuf. 5 (2015) 9–19, https://doi.org/10.1016/j.addma.2014.10.003.
[169] P. Åkerfeldt, M.L. Antti, R. Pederson, Influence of microstructure on mechanical properties of laser metal wire-deposited Ti-6Al-4V, Mater. Sci. Eng. A 674 (2016) 428–437, https://doi.org/10.1016/j.msea.2016.07.038.
[170] S.M.J. Razavi, F. Berto, Directed Energy Deposition versus Wrought Ti-6Al-4V: A Comparison of Microstructure, Fatigue Behavior, and Notch Sensitivity, Adv. Eng. Mater. 21 (8) (2019) 1900220, https://doi.org/10.1002/adem.201900220.
[171] D. Fu, X. Li, M. Zhang, M. Wang, Z. Zhang, S. Qu, Influence of effective laser energy on the structure and mechanical properties of laser melting deposited Ti6Al4V alloy, Materials 13 (4) (2020) 962, https://doi.org/10.3390/ma13040962.
[172] S. Liu, Y.C. Shin, Prediction of 3D microstructure and phase distributions of Ti6Al4V built by the directed energy deposition process via combined multi-physics models, Addit. Manuf. 34 (2020) 101234, https://doi.org/10.1016/j.addma.2020.101234.
[173] M. Shukla, R.M. Mahamood, E.T. Akinlabi, S. Pityana, Effect of Laser Power and Powder Flow Rate on Properties of Laser Metal Deposited Ti6Al4V, Int. J. Mech. Mechatron. Eng. 6 (11) (2012) 2475–2479, https://doi.org/10.5281/zenodo.1331915.
[174] A.W. Prabhu, T. Vincent, A. Chaudhary, W. Zhang, S.S. Babu, Effect of microstructure and defects on fatigue behaviour of directed energy deposited Ti–6Al–4V, Sci. Technol. Weld. Join. 20 (8) (2015) 659–669, https://doi.org/10.1179/1362171815Y.0000000050.
[175] Y.R. Choi, S.D. Sun, Q. Liu, M. Brandt, M. Qian, Influence of deposition strategy on the microstructure and fatigue properties of laser metal deposited Ti-6Al-4V powder on Ti-6Al-4V substrate, Int. J. Fatigue 130 (2020) 105236, https://doi.org/10.1016/j.ijfatigue.2019.105236.
[176] L. Yuan, S. Ding, C. Wen, Additive manufacturing technology for porous metal implant applications and triple minimal surface structures: A review, Bioact. Mater. 4 (2019) 56–70, https://doi.org/10.1016/j.bioactmat.2018.12.003.
[177] A.R. Nassar, J.S. Keist, E.W. Reutzel, T.J. Spurgeon, Intra-layer closed-loop control of build plan during directed energy additive manufacturing of Ti-6Al-4V, Addit. Manuf. 6 (2015) 39–52, https://doi.org/10.1016/j.addma.2015.03.005.
[178] Y. Zhai, H. Galarraga, D.A. Lados, Microstructure Evolution, Tensile Properties, and Fatigue Damage Mechanisms in Ti-6Al-4V Alloys Fabricated by Two Additive Manufacturing Techniques, Procedia Eng. 114 (2015) 658–666, https://doi.org/10.1016/j.proeng.2015.08.007.
[179] A.J. Sterling, B. Torries, N. Shamsaei, S.M. Thompson, D.W. Seely, Fatigue behavior and failure mechanisms of direct laser deposited Ti-6Al-4V, Mater. Sci. Eng. A 655 (2016) 100–112, https://doi.org/10.1016/j.msea.2015.12.026.
[180] H.R. Sandgren, Y. Zhai, D.A. Lados, P.A. Shade, J.C. Schuren, M.A. Groeber, P. Kenesei, A.G. Gavras, Characterization of fatigue crack growth behavior in LENS fabricated Ti-6Al-4V using high-energy synchrotron x-ray microtomography, Addit. Manuf. 12 (2016) 132–141, https://doi.org/10.1016/j.addma.2016.09.002.
[181] N.A. Kistler, D.J. Corbin, A.R. Nassar, E.W. Reutzel, A.M. Beese, Effect of processing conditions on the microstructure, porosity, and mechanical properties of Ti-6Al-4V repair fabricated by directed energy deposition, J. Mater. Process. Technol. 264 (2019) 172–181, https://doi.org/10.1016/j.jmatprotec.2018.08.041.
[182] S.M.J. Razavi, G.G. Bordonaro, P. Ferro, J. Torgersen, F. Berto, Fatigue behavior of porous Ti-6Al-4V made by laser-engineered net shaping, Materials 11 (2) (2018) 284, https://doi.org/10.3390/ma11020284.
[183] A. Fatemi, R. Molaei, S. Sharifimehr, N. Shamsaei, N. Phan, Torsional fatigue behavior of wrought and additive manufactured Ti-6Al-4V by powder bed fusion including surface finish effect, Int. J. Fatigue 99 (2017) 187–201, https://doi.org/10.1016/j.ijfatigue.2017.03.002.
[184] R. Konečná, L. Kunz, A. Bača, G. Nicoletto, Resistance of direct metal laser sintered Ti6Al4V alloy against growth of fatigue cracks, Eng. Fract. Mech. 185 (2017) 82–91, https://doi.org/10.1016/j.engfracmech.2017.03.033.
[185] P. Edwards, M. Ramulu, Fatigue performance evaluation of selective laser melted Ti-6Al-4V, Mater. Sci. Eng. A 598 (2014) 327–337, https://doi.org/10.1016/j.msea.2014.01.041.
[186] M. Waddell, K. Walker, R. Bandyopadhyay, K. Kapoor, A. Mallory, X. Xiao, A.C. Chuang, Q. Liu, N. Phan, M.D. Sangid, Small fatigue crack growth behavior of Ti-6Al-4V produced via selective laser melting: In situ characterization of a 3D crack tip interactions with defects, Int. J. Fatigue 137 (2020) 105638, https://doi.org/10.1016/j.ijfatigue.2020.105638.
[187] W. Xu, M. Brandt, S. Sun, J. Elambasseril, Q. Liu, K. Latham, K. Xia, M. Qian, Additive manufacturing of strong and ductile Ti-6Al-4V by selective laser melting via in situ martensite decomposition, Acta Mater. 85 (2015) 74–84, https://doi.org/10.1016/j.actamat.2014.11.028.
[188] K. Chang, E. Liang, W. Huang, X. Zhang, Y. Chen, J. Dong, R. Zhang, Microstructural feature and mechanical property in different building directions of additive manufactured Ti6Al4V alloy, Mater. Lett. 267 (2020) 127516, https://doi.org/10.1016/j.matlet.2020.127516.
[189] W. Sun, Y. Ma, W. Huang, W. Zhang, X. Qian, Effects of build direction on tensile and fatigue performance of selective laser melting Ti6Al4V titanium

alloy, Int. J. Fatigue 130 (2020) 105260, https://doi.org/10.1016/j.ijfatigue.2019.105260.
[190] Y.N. Hu, S.C. Wu, P.J. Withers, J. Zhang, H.Y.X. Bao, Y.N. Fu, G.Z. Kang, The effect of manufacturing defects on the fatigue life of selective laser melted Ti-6Al-4V structures, Mater. Des. 192 (2020) 108708, https://doi.org/10.1016/j.matdes.2020.108708.
[191] C. Chen, D. Gu, D. Dai, L. Du, R. Wang, C. Ma, M. Xia, Laser additive manufacturing of layered TiB2/Ti6Al4V multi-material parts: Understanding thermal behavior evolution, Opt. Laser Technol. 119 (2019) 105666, https://doi.org/10.1016/j.optlastec.2019.105666.
[192] A.M. Khorasani, I. Gibson, M. Goldberg, G. Littlefair, Production of Ti-6Al-4V acetabular shell using selective laser melting: Possible limitations in fabrication, Rapid Prototyp. J. 23 (1) (2017) 110–121, https://doi.org/10.1108/RPJ-11-2015-0159.
[193] N. Dai, L.C. Zhang, J. Zhang, Q. Chen, M. Wu, Corrosion behavior of selective laser melted Ti-6Al-4 V alloy in NaCl solution, Corros. Sci. 102 (2016) 484–489, https://doi.org/10.1016/j.corsci.2015.10.041.
[194] D.S. Nguyen, H.S. Park, C.M. Lee, Optimization of selective laser melting process parameters for Ti-6Al-4V alloy manufacturing using deep learning, J. Manuf. Process. 55 (2020) 230–235, https://doi.org/10.1016/j.jmapro.2020.04.014.
[195] K. Refai, C. Brugger, M. Montemurro, N. Saintier, An experimental and numerical study of the high cycle multiaxial fatigue strength of titanium lattice structures produced by Selective Laser Melting (SLM), Int. J. Fatigue 138 (2020) 105623, https://doi.org/10.1016/j.ijfatigue.2020.105623.
[196] Q. Yan, B. Chen, N. Kang, X. Lin, S. Lv, K. Kondoh, S. Li, J.S. Li, Comparison study on microstructure and mechanical properties of Ti-6Al-4V alloys fabricated by powder-based selective-laser-melting and sintering methods, Mater. Charact. 164 (2020) 110358, https://doi.org/10.1016/j.matchar.2020.110358.
[197] C. Ni, L. Zhu, Z. Zheng, J. Zhang, Y. Yang, R. Hong, Y. Bai, W.F. Lu, H. Wang, Effects of machining surface and laser beam scanning strategy on machinability of selective laser melted Ti6Al4V alloy in milling, Mater. Des. 194 (2020) 108880, https://doi.org/10.1016/j.matdes.2020.108880.
[198] Z. Chen, X. Yan, S. Yin, L. Liu, X. Liu, G. Zhao, W. Ma, W. Qi, Z. Ren, H. Liao, M. Liu, D. Cai, H. Fang, Influence of the pore size and porosity of selective laser melted Ti6Al4V ELI porous scaffold on cell proliferation, osteogenesis and bone ingrowth, Mater. Sci. Eng. C 106 (2020) 110289, https://doi.org/10.1016/j.msec.2019.110289.
[199] A. Arjunan, M. Demetriou, A. Baroutaji, C. Wang, Mechanical performance of highly permeable laser melted Ti6Al4V bone scaffolds, J. Mech. Behav. Biomed. Mater. 102 (2020) 103517, https://doi.org/10.1016/j.jmbbm.2019.103517.
[200] X. Yan, C. Shi, T. Liu, Y. Ye, C. Chang, W. Ma, C. Deng, S. Yin, H. Liao, M. Liu, Effect of heat treatment on the corrosion resistance behavior of selective laser melted Ti6Al4V ELI, Surf. Coat. Technol. 396 (2020) 125955, https://doi.org/10.1016/j.surfcoat.2020.125955.
[201] Special Metals, Inconel alloy 718 (2007).
[202] Special Metals, Inconel alloy 625 (2013).
[203] Y. Wang, J. Shi, Y. Liu, Competitive grain growth and dendrite morphology evolution in selective laser melting of Inconel 718 superalloy, J. Cryst. Growth 521 (2019) 15–29, https://doi.org/10.1016/j.jcrysgro.2019.05.027.
[204] The International Nickel Company Inc, Alloy IN-738 Technical Data (1981).
[205] D. Dye, O. Hunziker, S.M. Roberts, R.C. Reed, Modeling of the mechanical effects induced by the tungsten inert-gas welding of the IN718 superalloy, Metall. Mater. Trans. A 32 (7) (2001) 1713–1725, https://doi.org/10.1007/s11661-001-0149-z.
[206] X. Yin, G. He, W. Meng, Z. Xu, L. Hu, Q. Ma, Comparison Study of Low-Heat-Input Wire Arc-Fabricated Nickel-Based Alloy by Cold Metal Transfer and Plasma Arc, J. Mater. Eng. Perform. 29 (7) (2020) 4222–4232, https://doi.org/10.1007/s11665-020-04942-3.
[207] J.M. Kalinowski, Weldability of a Nickel-Based Superalloy, Contractor Report 195376, NASA (1994).
[208] B. Choudhury, M. Chandrasekaran, Electron beam welding of aerospace alloy (Inconel 825): A comparative study of RSM and ANN modeling to predict weld bead area, Optik 219 (2020) 165206, https://doi.org/10.1016/j.ijleo.2020.165206.
[209] K. Yuan, W. Guo, P. Li, J. Wang, Y. Su, X. Lin, Y. Li, Influence of process parameters and heat treatments on the microstructures and dynamic mechanical behaviors of Inconel 718 superalloy manufactured by laser metal deposition, Mater. Sci. Eng. A 721 (2018) 215–225, https://doi.org/10.1016/j.msea.2018.02.014.
[210] L.J. Kumar, C.G.K. Nair, Laser metal deposition repair applications for Inconel 718 alloy, Mater. Today: Proc. 4 (10) (2017) 11068–11077, https://doi.org/10.1016/j.matpr.2017.08.068.
[211] M. Fujishima, Y. Oda, R. Ashida, K. Takezawa, M. Kondo, Study on factors for pores and cladding shape in the deposition processes of Inconel 625 by the directed energy deposition (DED) method, CIRP J. Manuf. Sci. Technol. 19 (2017) 200–204, https://doi.org/10.1016/j.cirpj.2017.04.003.
[212] A.M. Kamara, S. Marimuthu, L. Li, Finite Element Modeling of Microstructure in Laser-Deposited Multiple Layer Inconel 718 Parts, Mater. Manuf. Process. 29 (10) (2014) 1245–1252, https://doi.org/10.1080/10426914.2014.930963.
[213] C. Zhong, J. Kittel, A. Gasser, J.H. Schleifenbaum, Study of nickel-based super-alloys Inconel 718 and Inconel 625 in high-deposition-rate laser metal deposition, Opt. Laser Technol. 109 (2019) 352–360, https://doi.org/10.1016/j.optlastec.2018.08.003.
[214] H. Rao, I. Jayasekara, B. Dutta, D. Maurice, Segregation phenomena during deposition of functionally graded zirconia-based ceramics with Stellite 21 on a steel substrate, Surf. Coat. Technol. 383 (2020) 125270, https://doi.org/10.1016/j.surfcoat.2019.125270.
[215] F. Liu, X. Lin, C. Huang, M. Song, G. Yang, J. Chen, W. Huang, The effect of laser scanning path on microstructures and mechanical properties of laser solid formed nickel-base superalloy Inconel 718, J. Alloy. Compd. 509 (13) (2011) 4505–4509, https://doi.org/10.1016/j.jallcom.2010.11.176.
[216] T.R. Walker, C.J. Bennett, T.L. Lee, A.T. Clare, A validated analytical-numerical modelling strategy to predict residual stresses in single-track laser deposited IN718, Int. J. Mech. Sci. 151 (2019) 609–621, https://doi.org/10.1016/j.ijmecsci.2018.12.004.
[217] M. Moda, B.D. Monelli, M. Benassi, M. Palladino, Validation of a multi-scale simulation strategy based on the Pointwise Strain Superposition Method, IOP Conf. Ser.: Mater. Sci. Eng. 1038 (1) (2021) 012022, https://doi.org/10.1088/1757-899X/1038/1/012022.
[218] C. Pei, D. Shi, H. Yuan, H. Li, Assessment of mechanical properties and fatigue performance of a selective laser melted nickel-base superalloy Inconel 718, Mater. Sci. Eng. A 759 (2019) 278–287, https://doi.org/10.1016/j.msea.2019.05.007.
[219] W.M. Tucho, P. Cuvillier, A. Sjolyst-Kverneland, V. Hansen, Microstructure and hardness studies of Inconel 718 manufactured by selective laser melting before and after solution heat treatment, Mater. Sci. Eng. A 689 (2017) 220–232, https://doi.org/10.1016/j.msea.2017.02.062.
[220] M. Calandri, S. Yin, B. Aldwell, F. Calignano, R. Lupoi, D. Ugues, Texture and microstructural features at different length scales in Inconel 718 produced by selective laser melting, Materials 12 (8) (2019) 1293, https://doi.org/10.3390/ma12081293.
[221] R. Barros, F.J.G. Silva, R.M. Gouveia, A. Saboori, G. Marchese, S. Biamino, A. Salmi, E. Atzeni, Laser Powder Bed Fusion of Inconel 718: Residual Stress Analysis Before and After Heat Treatment, Metals 9 (12) (2019) 1290, https://doi.org/10.3390/met9121290.
[222] Y. Cao, P. Bai, F. Liu, X. Hou, Y. Guo, Effect of the solution temperature on the precipitates and grain evolution of IN718 fabricated by laser additive manufacturing, Materials 13 (2) (2020) 340, https://doi.org/10.3390/ma13020340.
[223] Y. Lu, S. Wu, Y. Gan, T. Huang, C. Yang, L. Junjie, J. Lin, Study on the microstructure, mechanical property and residual stress of SLM Inconel-718 alloy manufactured by differing island scanning strategy, Opt. Laser Technol. 75 (2015) 197–206, https://doi.org/10.1016/j.optlastec.2015.07.009.
[224] A.J. Dunbar, E.R. Denlinger, J. Heigel, P. Michaleris, P. Guerrier, R. Martukanitz, T.W. Simpson, Development of experimental method for in situ distortion and temperature measurements during the laser powder bed fusion additive manufacturing process, Addit. Manuf. 12 (2016) 25–30, https://doi.org/10.1016/j.addma.2016.04.007.
[225] D.S. Watring, K.C. Carter, D. Crouse, B. Raeymaekers, A.D. Spear, Mechanisms driving high-cycle fatigue life of as-built Inconel 718 processed by laser powder bed fusion, Mater. Sci. Eng. A 761 (2019) 137993, https://doi.org/10.1016/j.msea.2019.06.003.
[226] I. Yadroitsev, M. Pavlov, P. Bertrand, I. Smurov, Mechanical properties of samples fabricated by selective laser melting, 14èmes Assises Européennes du Prototypage & Fabrication Rapide 625 (2009) 24–25.
[227] M.A. Anam, D. Pal, B. Stucker, Modeling and Experimental validation of Nickel-based super alloy (Inconel 625) made using Selective Laser Melting, 24th International Solid Freeform Fabrication Symposium (2013) 463–473, https://doi.org/10.13140/2.1.4009.1201.
[228] G. Marchese, X. Garmendia Colera, F. Calignano, M. Lorusso, S. Biamino, P. Minetola, D. Manfredi, Characterization and Comparison of Inconel 625 Processed by Selective Laser Melting and Laser Metal Deposition, Adv. Eng. Mater. 19 (3) (2017) 1600635, https://doi.org/10.1002/adem.201600635.
[229] M. Scurria, B. Möller, R. Wagener, J. Pena, T. Bein, Effects of Surface Preparation, Support Structures and Build Orientation on the Cyclic Stress-Strain Behavior of Inconel 718 Produced by SLM, SAE Technical Paper (2019) 2019-01-0918, https://doi.org/10.4271/2019-01-0918.
[230] S.Y. Liu, H.Q. Li, C.X. Qin, R. Zong, X.Y. Fang, The effect of energy density on texture and mechanical anisotropy in selective laser melted Inconel 718, Mater. Des. 191 (2020) 108642, https://doi.org/10.1016/j.matdes.2020.108642.
[231] T.D. McLouth, D.B. Witkin, G.E. Bean, S.D. Sitzman, P.M. Adams, J.R. Lohser, J. M. Yang, R.J. Zaldivar, Variations in ambient and elevated temperature mechanical behavior of IN718 manufactured by selective laser melting via process parameter control, Mater. Sci. Eng. A 780 (2020) 139184, https://doi.org/10.1016/j.msea.2020.139184.
[232] D.A. Lesyk, S. Martinez, B.N. Mordyuk, V.V. Dzhemelinskyi, A. Lamikiz, G.I. Prokopenko, Post-processing of the Inconel 718 alloy parts fabricated by selective laser melting: Effects of mechanical surface treatments on surface topography, porosity, hardness and residual stress, Surf. Coat. Technol. 381 (2020) 125136, https://doi.org/10.1016/j.surfcoat.2019.125136.
[233] C. Chen, J. Yin, H. Zhu, X. Zeng, G. Wang, L. Ke, J. Zhu, S. Chang, The effect of process parameters on the residual stress of selective laser melted Inconel 718 thin-walled part, Rapid Prototyp. J. 25 (8) (2019) 1359–1369, https://doi.org/10.1108/RPJ-09-2018-0249.
[234] S. Luo, W. Huang, H. Yang, J. Yang, Z. Wang, X. Zeng, Microstructural evolution and corrosion behaviors of Inconel 718 alloy produced by selective laser melting following different heat treatments, Addit. Manuf. 30 (2019) 100875, https://doi.org/10.1016/j.addma.2019.100875.

[235] X.F. Ma, H.L. Zhai, L. Zuo, W.J. Zhang, S.S. Rui, Q.N. Han, J.S. Jiang, C.P. Li, G.F. Chen, G.A. Qian, S.J. Zhao, Fatigue short crack propagation behavior of selective laser melted Inconel 718 alloy by in-situ SEM study: Influence of orientation and temperature, Int. J. Fatigue 139 (2020) 105739, https://doi.org/10.1016/j.ijfatigue.2020.105739.

[236] M. Sadowski, L. Ladani, W. Brindley, J. Romano, Optimizing quality of additively manufactured Inconel 718 using powder bed laser melting process, Addit. Manuf. 11 (2016) 60–70, https://doi.org/10.1016/j.addma.2016.03.006.

[237] V.A. Popovich, E.V. Borisov, A.A. Popovich, V.S. Sufiiarov, D.V. Masaylo, L. Alzina, Functionally graded Inconel 718 processed by additive manufacturing: Crystallographic texture, anisotropy of microstructure and mechanical properties, Mater. Des. 114 (2017) 441–449, https://doi.org/10.1016/j.matdes.2016.10.075.

[238] C. Guo, S. Li, S. Shi, X. Li, X. Hu, Q. Zhu, R.M. Ward, Effect of processing parameters on surface roughness, porosity and cracking of as-built IN738LC parts fabricated by laser powder bed fusion, J. Mater. Process. Technol. 285 (2020) 116788, https://doi.org/10.1016/j.jmatprotec.2020.116788.

[239] M. Balbaa, S. Mekhiel, M. Elbestawi, J. McIsaac, On selective laser melting of Inconel 718: Densification, surface roughness, and residual stresses, Mater. Des. 193 (2020) 108818, https://doi.org/10.1016/j.matdes.2020.108818.

[240] B.B. Ravichander, A. Amerinatanzi, N. Shayesteh Moghaddam, Study on the Effect of Powder-Bed Fusion Process Parameters on the Quality of as-Built IN718 Parts Using Response Surface Methodology, Metals 10 (9) (2020) 1180, https://doi.org/10.3390/met10091180.

[241] M. Leary, M. Mazur, H. Williams, E. Yang, A. Alghamdi, B. Lozanovski, X. Zhang, D. Shidid, L. Farahbod-Sternahl, G. Witt, I. Kelbassa, P. Choong, M. Qian, M. Brandt, Inconel 625 lattice structures manufactured by selective laser melting (SLM): Mechanical properties, deformation and failure modes, Mater. Des. 157 (2018) 179–199, https://doi.org/10.1016/j.matdes.2018.06.010.

[242] L. Alter, A. Heider, J.P. Bergmann, Investigations on copper welding using a frequency-doubled disk laser and high welding speeds, Procedia CIRP 74 (2018) 12–16, https://doi.org/10.1016/j.procir.2018.08.003.

[243] J. Freudenberger, H. Warlimont, Copper and Copper Alloys, Springer Handbook of Materials Data (2018) 297–305, https://doi.org/10.1007/978-3-319-69743-7_12.

[244] Metalcor GmbH, CuCr1Zr Datasheet (2020).

[245] L.J. Zhang, Q.L. Bai, J. Ning, A. Wang, J.N. Yang, X.Q. Yin, J.X. Zhang, A comparative study on the microstructure and properties of copper joint between MIG welding and laser-MIG hybrid welding, Mater. Des. 110 (2016) 35–50, https://doi.org/10.1016/j.matdes.2016.07.117.

[246] L.J. Zhang, J. Ning, X.J. Zhang, G.F. Zhang, J.X. Zhang, Single pass hybrid laser-MIG welding of 4-mm thick copper without preheating, Mater. Des. 74 (2015) 1–18, https://doi.org/10.1016/j.matdes.2015.02.027.

[247] J.N. Yang, L.J. Zhang, J. Ning, Q.L. Bai, X.Q. Yin, J.X. Zhang, Single-pass hybrid laser-MIG welding of 8-mm-thick pure copper (T2) without preheating: weld geometry and integrity, Int. J. Adv. Manuf. Technol. 91 (9) (2017) 3749–3773, https://doi.org/10.1007/s00170-017-0083-x.

[248] J. Ning, L.J. Zhang, A. Wang, Q.L. Bai, J.N. Yang, J.X. Zhang, Effects of double-pass welding and extrusion on properties of fiber laser welded 1.5-mm thick T2 copper joints, J. Mater. Process. Technol. 237 (2016) 75–87, https://doi.org/10.1016/j.jmatprotec.2016.06.011.

[249] J. Yang, F. Wu, B. Bai, G. Wang, L. Yang, S. Zhou, J. Lei, Effect of Cr additions on the microstructure and corrosion resistance of Diode laser clad CuAl10 coating, Surf. Coat. Technol. 381 (2020) 125215, https://doi.org/10.1016/j.surfcoat.2019.125215.

[250] F. Arias-González, J. del Val, R. Comesaña, J. Penide, F. Lusquiños, F. Quintero, A. Riveiro, M. Boutinguiza, J. Pou, Laser cladding of phosphor bronze, Surf. Coat. Technol. 313 (2017) 248–254, https://doi.org/10.1016/j.surfcoat.2017.01.097.

[251] M. Samodurova, N. Shaburova, O. Samoilova, L. Radionova, R. Zakirov, K. Pashkeev, V. Myasoedov, I. Erdakov, E. Trofimov, A study of characteristics of aluminum bronze coatings applied to steel using additive technologies, Materials 13 (2) (2020) 461, https://doi.org/10.3390/ma13020461.

[252] Z. Ma, D.Z. Zhang, F. Liu, J. Jiang, M. Zhao, T. Zhang, Lattice structures of Cu-Cr-Zr copper alloy by selective laser melting: Microstructures, mechanical properties and energy absorption, Mater. Des. 187 (2020) 108406, https://doi.org/10.1016/j.matdes.2019.108406.

[253] Z. Ma, K. Zhang, Z. Ren, D.Z. Zhang, G. Tao, H. Xu, Selective laser melting of Cu-Cr-Zr copper alloy: Parameter optimization, microstructure and mechanical properties, J. Alloy. Compd. 828 (2020) 154350, https://doi.org/10.1016/j.jallcom.2020.154350.

[254] G. Zhang, S. Liu, C. Chen, X. Zhang, X. Gan, Q. Lei, Z. Li, K. Zhou, Effect of heat treatment on microstructure and mechanical properties of a selective laser melted Cu-15Ni-8Sn alloy, Mater. Sci. Eng. A 763 (2019) 138132, https://doi.org/10.1016/j.msea.2019.138132.

[255] Y. Chen, S. Ren, Y. Zhao, X. Qu, Microstructure and properties of CuCr alloy manufactured by selective laser melting, J. Alloy. Compd. 786 (2019) 189–197, https://doi.org/10.1016/j.jallcom.2019.01.179.

[256] Z. Tan, X. Zhang, Z. Zhou, Z. Zhou, Y. Yang, X. Guo, Z. Wang, X. Wu, G. Wang, D. He, Thermal effect on the microstructure of the lattice structure Cu-10Sn alloy fabricated through selective laser melting, J. Alloy. Compd. 787 (2019) 903–908, https://doi.org/10.1016/j.jallcom.2019.02.196.

[257] T.T. Ikeshoji, K. Nakamura, M. Yonehara, K. Imai, H. Kyogoku, Selective Laser Melting of Pure Copper, JOM 70 (3) (2018) 396–400, https://doi.org/10.1007/s11837-017-2695-x.

[258] S. Uchida, T. Kimura, T. Nakamoto, T. Ozaki, T. Miki, M. Takemura, Y. Oka, R. Tsubota, Microstructures and electrical and mechanical properties of Cu-Cr alloys fabricated by selective laser melting, Mater. Des. 175 (2019) 107815, https://doi.org/10.1016/j.matdes.2019.107815.

[259] Y.K. Kim, S.H. Park, K.A. Lee, Effect of post-heat treatment on the thermophysical and compressive mechanical properties of Cu-Ni-Sn alloy manufactured by selective laser melting, Mater. Charact. 162 (2020) 110194, https://doi.org/10.1016/j.matchar.2020.110194.

[260] C. Wallis, B. Buchmayr, Effect of heat treatments on microstructure and properties of CuCrZr produced by laser-powder bed fusion, Mater. Sci. Eng. A 744 (2019) 215–223, https://doi.org/10.1016/j.msea.2018.12.017.

[261] S.D. Jadhav, S. Dadbakhsh, L. Goossens, J.P. Kruth, J. Van Humbeeck, K. Vanmeensel, Influence of selective laser melting process parameters on texture evolution in pure copper, J. Mater. Process. Technol. 270 (2019) 47–58, https://doi.org/10.1016/j.jmatprotec.2019.02.022.

[262] S. Scudino, C. Unterdörfer, K.G. Prashanth, H. Attar, N. Ellendt, V. Uhlenwinkel, J. Eckert, Additive manufacturing of Cu-10Sn bronze, Mater. Lett. 156 (2015) 202–204, https://doi.org/10.1016/j.matlet.2015.05.076.

[263] S.D. Jadhav, S. Dadbakhsh, R. Chen, R. Shabadi, J.P. Kruth, J. Van Humbeeck, K. Vanmeensel, Modification of Electrical and Mechanical Properties of Selective Laser-Melted CuCr0.3 Alloy Using Carbon Nanoparticles, Adv. Eng. Mater. 22 (2) (2020) 1900946, https://doi.org/10.1002/adem.201900946.

[264] K. Jahns, R. Bappert, P. Böhlke, U. Krupp, Additive manufacturing of CuCr1Zr by development of a gas atomization and laser powder bed fusion routine, Int. J. Adv. Manuf. Technol. 107 (5) (2020) 2151–2161, https://doi.org/10.1007/s00170-020-04941-7.

[265] J. Huang, X. Yan, C. Chang, Y. Xie, W. Ma, R. Huang, R. Zhao, S. Li, M. Liu, H. Liao, Pure copper components fabricated by cold spray (CS) and selective laser melting (SLM) technology, Surf. Coat. Technol. 395 (2020) 125936, https://doi.org/10.1016/j.surfcoat.2020.125936.

[266] B. Buchmayr, G. Panzl, A. Walzl, C. Wallis, Laser Powder Bed Fusion – Materials Issues and Optimized Processing Parameters for Tool steels, AlSiMg- and CuCrZr-Alloys, Adv. Eng. Mater. 19 (4) (2017) 1600667, https://doi.org/10.1002/adem.201600667.

[267] M. Colopi, L. Caprio, A.G. Demir, B. Previtali, Selective laser melting of pure Cu with a 1 kW single mode fiber laser, Procedia CIRP 74 (2018) 59–63, https://doi.org/10.1016/j.procir.2018.08.030.

[268] P. Guan, X. Chen, P. Liu, F. Sun, C. Zhu, H. Zhou, S. Fu, Z. Wu, Y. Zhu, Effect of selective laser melting process parameters and aging heat treatment on properties of CuCrZr alloy, Mater. Res. Express 6 (11) (2019) 1165c1, https://doi.org/10.1088/2053-1591/ab4e2f.

[269] Z. Mao, D.Z. Zhang, J. Jiang, G. Fu, P. Zhang, Processing optimisation, mechanical properties and microstructural evolution during selective laser melting of Cu-15Sn high-tin bronze, Mater. Sci. Eng. A 721 (2018) 125–134, https://doi.org/10.1016/j.msea.2018.02.051.

[270] E. Uhlmann, A.E. Tekkaya, V. Kashevko, S. Gies, R. Reimann, P. John, Qualification of CuCr1Zr for the SLM Process, Proceedings of the 7th International Conference on High Speed Forming (2016) 173–182, https://doi.org/10.17877/DE290R-16984.

[271] Y. Zhao, Y. Koizumi, K. Aoyagi, D. Wei, K. Yamanaka, A. Chiba, Molten pool behavior and effect of fluid flow on solidification conditions in selective electron beam melting (SEBM) of a biomedical Co-Cr-Mo alloy, Addit. Manuf. 26 (2019) 202–214, https://doi.org/10.1016/j.addma.2018.12.002.

[272] D.G. Farwick, R.N. Johnson, Thermophysical properties of selected wear-resistant alloys, Tech. Rep. HEDL-TME-79-6, Hanford Engineering Development Lab. (1980).

[273] R. Rocha, A.L.B. Pinheiro, A.B. Villaverde, Flexural strength of pure Ti, Ni-Cr and Co-Cr alloys submitted to Nd:YAG laser or TIG welding, Braz. Dent. J. 17 (1) (2006) 20–23, https://doi.org/10.1590/S0103-64402006000100005.

[274] A. Shahroozi, A. Afsari, B. Khakan, A.R. Khalifeh, Microstructure and mechanical properties investigation of stellite 6 and Stellite 6/TiC coating on ASTM A105 steel produced by TIG welding process, Surf. Coat. Technol. 350 (2018) 648–658, https://doi.org/10.1016/j.surfcoat.2018.07.044.

[275] A. Prakash, A.S. Shahi, Investigations on high temperature wear and metallurgical characteristics of Stellite 6 GTA (Gas Tungsten Arc) weld claddings, Mater. Res. Express 7 (2) (2020) 026509, https://doi.org/10.1088/2053-1591/ab6e2b.

[276] G.P. Rajeev, M. Kamaraj, S.R. Bakshi, Comparison of microstructure, dilution and wear behavior of Stellite 21 hardfacing on H13 steel using cold metal transfer and plasma transferred arc welding processes, Surf. Coat. Technol. 375 (2019) 383–394, https://doi.org/10.1016/j.surfcoat.2019.07.019.

[277] J. Foster, C. Cullen, S. Fitzpatrick, G. Payne, L. Hall, J. Marashi, Remanufacture of hot forging tools and dies using laser metal deposition with powder and a hard-facing alloy Stellite 21, J. Remanufactur. 9 (3) (2019) 189–203, https://doi.org/10.1007/s13243-018-0063-9.

[278] M. Moradi, A. Ashoori, A. Hasani, Additive manufacturing of stellite 6 superalloy by direct laser metal deposition – Part 1: Effects of laser power and focal plane position, Opt. Laser Technol. 131 (2020) 106328, https://doi.org/10.1016/j.optlastec.2020.106328.

[279] K.D. Traxel, A. Bandyopadhyay, First Demonstration of Additive Manufacturing of Cutting Tools using Directed Energy Deposition System: Stellite-Based Cutting Tools, Addit. Manuf. 25 (2019) 460–468, https://doi.org/10.1016/j.addma.2018.11.019.

[280] M. Dahmen, M. Göbel, Mechanical properties and fracture behaviour of LMD produced 2.4682 and wrought 2.4630 dissimilar welds, Phys. Procedia 83 (2016) 426–436, https://doi.org/10.1016/j.phpro.2016.08.044.
[281] A. Sadhu, D. Patra Karmakar, O. Mypati, G. Muvvala, S.K. Pal, A.K. Nath, Performance of additive manufactured Stellite 6 tools in friction stir processing of CuCrZr sheet, Opt. Laser Technol. 128 (2020) 106241, https://doi.org/10.1016/j.optlastec.2020.106241.
[282] K. Li, X. Mao, K. Khanlari, K. Song, Q. Shi, X. Liu, Effects of powder size distribution on the microstructural and mechanical properties of a Co-Cr-W-Si alloy fabricated by selective laser melting, J. Alloy. Compd. 825 (2020) 153973, https://doi.org/10.1016/j.jallcom.2020.153973.
[283] H. Wang, J. Xu, Z. Nie, W. Ma, Q. Zhang, L. Guo, Preparation and properties of Co-Cr alloy denture by selective laser melting, Mater. Res. Express 6 (2) (2019) 026552, https://doi.org/10.1088/2053-1591/aaee5d.
[284] K.S. Kim, J.W. Hwang, K.A. Lee, Effect of building direction on the mechanical anisotropy of biocompatible Co-Cr-Mo alloy manufactured by selective laser melting process, J. Alloy. Compd. 834 (2020) 155055, https://doi.org/10.1016/j.jallcom.2020.155055.
[285] C. Teng, H. Gong, A. Szabo, J.J.S. Dilip, K. Ashby, S. Zhang, N. Patil, D. Pal, B. Stucker, Simulating Melt Pool Shape and Lack of Fusion Porosity for Selective Laser Melting of Cobalt Chromium Components, J. Manuf. Sci. Eng. 139 (1) (2017) 011009, https://doi.org/10.1115/1.4034137.
[286] V. Finazzi, A.G. Demir, C.A. Biffi, F. Migliavacca, L. Petrini, B. Previtali, Design and functional testing of a novel balloon-expandable cardiovascular stent in CoCr alloy produced by selective laser melting, J. Manuf. Process. 55 (2020) 161–173, https://doi.org/10.1016/j.jmapro.2020.03.060.
[287] Y. Lu, C. Yang, Y. Liu, K. Yang, J. Lin, Characterization of lattice defects and tensile deformation of biomedical Co29Cr9W3Cu alloy produced by selective laser melting, Addit. Manuf. 30 (2019) 100908, https://doi.org/10.1016/j.addma.2019.100908.
[288] A.G. Demir, B. Previtali, Additive manufacturing of cardiovascular CoCr stents by selective laser melting, Mater. Des. 119 (2017) 338–350, https://doi.org/10.1016/j.matdes.2017.01.091.
[289] T. Qi, H. Zhu, X. Zeng, J. Yin, Effect of Si content on the cracking behavior of selective laser melted Al7050, Rapid Prototyp. J. 25 (10) (2019) 1592–1600, https://doi.org/10.1108/RPJ-12-2018-0310.
[290] International Standards, ASTM F3055-14a(2021) Standard Specification for Additive Manufacturing Nickel Alloy (UNS N07718) with Powder Bed Fusion, ASTM International, West Conshohocken, US-PA, 2021.
[291] A.S. Agazhanov, D.A. Samoshkin, Y.M. Kozlovskii, Thermophysical properties of Inconel 718 alloy, J. Phys.: Conf. Ser. 1382 (1) (2019) 012175, https://doi.org/10.1088/1742-6596/1382/1/012175.
[292] Y.H. Zhou, Z.H. Zhang, Y.P. Wang, G. Liu, S.Y. Zhou, Y.L. Li, J. Shen, M. Yan, Selective laser melting of typical metallic materials: An effective process prediction model developed by energy absorption and consumption analysis, Addit. Manuf. 25 (2019) 204–217, https://doi.org/10.1016/j.addma.2018.10.046.